Ocean Modelling 119 (2017) 118–135

Contents lists available at ScienceDirect

Ocean Modelling

journal homepage: www.elsevier.com/locate/ocemod

Rotating 2d point source plume models with application to Deepwater Horizon

A. Fabregat[a], B. Deremble[b], N. Wienders[b], A. Stroman[b], A. Poje[a], T.M. Özgökmen[c], W.K. Dewar[*,b]

[a] Dept. of Mathematics, CUNY-Staten Island, NY, 10314, United States
[b] Dept. of EOAS, Florida State University, Tallahassee, FL, 32309, United States
[c] Dept. of Ocean Sciences, RSMAS, Miami, FL, 33149, United States

ARTICLE INFO

Keywords:
Multi-phase plumes with rotation
2-D/3-D comparisons

ABSTRACT

The 2010 Deepwater Horizon (DwH) accident in the Gulf of Mexico has renewed oceanographic interest in point source buoyant convection. The present paper applies modern numerical techniques to study this problem, focussing specifically on the DwH event. The gas/oil/seawater nature of the problem requires a 'multiphase' approach, which is relatively unfamiliar in physical oceanography, although applications are becoming more common. The model is cast in an Eulerian framework and includes feedbacks between the convection and the environment, unlike past oil/gas plume simulations that adopt a semi-passive, Lagrangian approach. Fully three dimensional (3d) simulations are too computationally demanding for practical multi-day use, so a two-dimensional (2d) radially symmetric model is developed from the equations and calibrated to the 3d results. Both the 2d and 3d solutions show the somewhat unexpected result that oil/bubble plumes modelled after the DwH event are strongly affected by rotation and exert a considerable dynamic feedback on the ambient. These effects are not typically included in classical oil/gas plume models.

1. Introduction

At 9:45PM, April 20, 2010, an explosion occurred on the Deepwater Horizon drilling rig, located in the Gulf of Mexico, killing 11 people and injuring 17 others (Graham et al., 2011). This was the beginning of the Deepwater Horizon accident, an event that lasted for 87 days. The spill went through several phases: the initial phase where the deep pipe leaked from two locations, the phase where the riser pipe was cut, localizing the spill to the wellhead and last, additions of various diffusers and dispersants at the wellhead (Plume Modeling Team, 2010). The effluent was a mixture of so-called 'Macondo Oil' and gases (primarily methane). The oil, itself a mixture of several different hydrocarbons (Reddy et al., 2012), constitutes an independent material from the water and is largely immiscible with it. The gas is also an independent phase but is more likely to be consumed and to dissolve into the seawater. The discharge was large (4.9 million barrels of oil and about 5.3 million barrels of gas, (Lehr et al., 2010)) and considerable effort went into oil recovery, burning of surface oil and clean up of beaches dirtied by oil.

If recent history is a guide, deep-ocean oil drilling efforts will increase. Taking the above parameters as representative of an 'average' spill, an accident is a major event. As such, there exists a pressing need to better understand the biological, chemical and physical fate of the oil, its spreading rate, and its impact on the environment. This paper describes and analyzes a somewhat novel approach to near-field deep ocean oil plume modelling based on an Eulerian representation that, while more computationally demanding, promises some advantages relative to the more classical Lagrangian based models. A separate and more practical advantage is this design fits seamlessly within an existing ocean general circulation model that can support future oil spill tracking.

1.1. Background

Buoyant, turbulent plumes have a literature spanning several decades. Zeldovich (1937) and Schmidt (1941) conducted early dimensional analyses yielding scaling laws for various plume measures. Batchelor (1954), Morton et al. (1956) and Turner in a series of papers (see Turner, 1973 and references therein) performed several analytical and laboratory plume studies. Observations and numerical work on plumes were combined in Zaker et al. (2001) and stratified plume experimental results appear in List and Imberger (1973). Well-posed extensions of the Morton et al. (1956) models to unsteady settings have recently been advanced by Scase and Hewitt (2012) and Craske and van

* Corresponding author.
E-mail addresses: wdewar@fsu.edu, dewar@ocean.fsu.edu (W.K. Dewar).

http://dx.doi.org/10.1016/j.ocemod.2017.10.005
Received 23 September 2016; Received in revised form 12 October 2017; Accepted 15 October 2017
Available online 16 October 2017
1463-5003/

Reeuwijk (2016). Motivated by convection in deep ocean thermal vents, Speer and Marshall (1995) derived scaling laws for plumes evolving in the presence of rotation and stratification. As argued by Woods and Bush (1999), the observations by D'Asaro et al. (1994) are consistent with much of the proposed scaling,

McDougall (1978) performed early bubble plume experiments and emphasized their effect on neutral level intrusions. Asaeda and Imberger (1993) classified two-phase plumes into three types depending upon the number of spreading levels and the strength of the bubble flux (see also Lemckert and Imberger, 1993). Socolofsky and Adams (2002) and Socolofsky and Adams (2005) present more recent non-rotating laboratory bubble plume experiments, emphasizing the importance of the nondimensional group characterizing the relative slip velocity of the gas phase.

Helfrich and Battisti (1991) conducted a series of buoyant release experiments, at various Rossby numbers, to investigate the effects of system rotation on the long-time behavior of stratified plumes. The numerical plume simulations in Speer and Marshall (1995) identified a strong cyclonic circulation at the plume base and a much weaker anticyclonic current at the lateral intrusion, both of which appeared in the Helfrich and Battisti (1991) experiments. Momentum and energy budget analysis of turbulent resolving simulations in Fabregat et al. (2016a) explained other rotation effects observed in Helfrich and Battisti (1991), including a decrease in trapping height and an increase in the thickness of the lateral intrusion layer.

Environmental modelling of multiphase plume has, historically, typically been conducted in the Lagrangian frame. Particles representing oil droplets and gas bubbles with evolving physio-chemical properties are advected by an imposed background flow field. Two such models, the Comprehensive Deepwater Oil and Gas model (CDOG, (Zheng et al., 2003)) and DeepBlow (Johansen, 2000), have been directly tested against field experiments. A second Lagrangian type approach has been to compute the trajectory of integral plume measures, e.g. the centerline location and the plume width (Socolofsky et al., 2008).

Socolofsky et al. (2011) applied simple models of this type to the DwH event focussing on the importance of the regional stratification.

Socolofsky et al. (2015) describe, in detail, intercomparisons of several Lagrangian models applied to the DwH event.

A turbulence resolving model similar to the one used here (described in the next section) was recently applied to plumes in a thermally stratified environment and forced either by heat, gas or a combination of heat and gas (Fabregat et al., 2015; 2016a; 2016b). The overall plume topology dependence on the gas phase slip velocity observed in the Socolofsky and Adams (2002); 2005) experiments was successfully reproduced in these simulations. Both rotating and non-rotating settings were examined. They argued that rotating multiphase plumes differed significantly from non-rotating ones in several ways, including effects on the turbulence and precession of the plume axis.

1.2. The DwH event in context

Oil and gas are both buoyant in seawater. While Macondo oil density estimates at 1500 m vary, from a low of 670 kg/m^3 (Plume Calculation Team, 2010) to 840 kg/m^3 (Liu, et al., 2012; Socolofsky et al., 2011), it is clearly light relative to the ambient seawater with density 1035 kg/m^3. Methane density at these pressures and temperatures is roughly 100 kg/m^3 (http://yeroc.us/calculators/gas-density.php). Thus, the buoyancy fluxes at the DwH wellhead are, by oceanographic standards, astounding. The oil-gas mixture (approximately half oil and half gas) exited the well at roughly 2 m/s ((Plume Modeling Team, 2010)). Considering only the oil, and using the smaller oil density anamoly, the DwH buoyancy flux was $B_f = 2$ m^2 s^{-3}. As a yardstick for evaluating this flux, to produce it with seawater would require

$$\frac{\rho_o B_f C_p}{g\gamma} = \frac{10^3\ \text{Kg}}{\text{m}^3}\ \frac{2\ \text{m}^2}{\text{s}^{-3}}\ \frac{4\times 10^3\ \text{J}}{\text{Kg K}}\ \frac{s^2}{10\ \text{m}}\ \frac{K}{2\times 10^{-4}} = 4\times 10^9\ \frac{\text{W}}{\text{m}^2} = 4\ \text{GW m}^{-2} \quad (1)$$

where C_p is seawater heat capacity, g gravity and γ the coefficient of thermal expansion for water. We ignore the fact that the equation of state would surely break down in these circumstances.

The largest buoyancy fluxes associated with cold air outbreaks over the Gulf Stream are 1000 W m^{-2} (Joyce and Stalcup, 1985) and last for a few hours, as compared to the the 87 day long DwH event. The DwH flux is large even in comparison to hydrothermal vents, which are 100–1000 times weaker (Speer and Marshall, 1995). Allowing for the methane in the plume, net buoyancy flux increases by a factor of 6. Accounting for the size of the vent, the total power output becomes 3×10^9 W. In contrast, the buoyancy flux associated with individual deep sea vents are typically estimated to be $10^6 - 10^7$ W while collections of vents may produce fluxes approaching 2.2×10^8 W.

1.3. This paper

Our interests are in complementing the above Lagrangian/integral multiphase plume models by exploiting modern computational techniques. We develop an Eulerian based multiphase near-field model including explicit turbulence representation. The associated fluid dynamics are very general, thereby allowing for rotation, feedback of the plume on the environment and an evolving background environment. Written in the Eulerian frame, the plume model is readily incorporated as a sub-component within existing general circulation ocean models.

Given that much (15%–30%) of the DwH oil remained subsurface (Lubchenco et al., 2012; McNutt et al., 2012), there is a clear need to understand the detailed evolution of oil within the plume. Knowledge of how and where in the water column the oil detrains and its long term fate is important to assessing subsurface oil ecosystem impacts. It is hoped the present model will be the foundation for a next-generation end-to-end oil spill assessment tool.

The next section presents our model in the form of partial differential equations. These are abstracted from discrete statements obtained through a volume integration approach to multiphase fluid dynamics. The derivation of the discrete set is given in the Appendix, along with a brief discussion of the parameterizations necessary to arrive at the continuous model. We compare two-dimensional (2d) and three-dimensional (3d) models based on these equations for the purpose of assessing the accuracy of the 2d model. The 2d model is then used to estimate the long-term, multi-day structure of the DwH plume. We conclude with a summary and future work discussion.

Our 2d model compares reasonably well to non-rotating 3d results. While much of the qualitative plume structure appears in our 2d model for thermal plumes, the presence of a slipping gas phase degrades the 2d-3d comparisons considerably. As such, the rotating thermal plume model is used to explore long-time (several rotation periods) evolution in order to qualitatively illustrate how the DwH plume in a rotational setting differs from the non-rotating case. We argue the effects of rotation are sufficiently strong that they appear in spite of quantitative model shortcomings. It is our opinion that the results emphasize the importance of exploring other physics normally recognized as of leading order importance, such as cross flow and time variable background fields, in the presence of rotation.

2. Multiphase equations and simulations

The equations for a three-phase (oil, gas, water) fluid in a rotating, stratified setting are

$$\begin{aligned}
\frac{\partial}{\partial t}\boldsymbol{u} + \boldsymbol{u}\cdot\nabla\boldsymbol{u} + 2\boldsymbol{\Omega}\times\boldsymbol{u} &= -\nabla p + B\boldsymbol{k} + \nabla\cdot\nu^{visc}\nabla\boldsymbol{u} \\
\nabla\cdot\boldsymbol{u} &= 0 \\
\frac{\partial}{\partial t}T + \nabla\cdot\boldsymbol{u}T &= F^{T} \\
\alpha_{oil} + \alpha_{water} &= 1 \\
\frac{\partial}{\partial t}(\alpha_{oil}) + \nabla\cdot\boldsymbol{u}_{oil}\alpha_{oil} &= F^{\alpha_{oil}} \\
\frac{\partial}{\partial t}(M_{gas}) + \nabla\cdot\boldsymbol{u}_{\boldsymbol{gas}}M_{gas} &= F^{M_{gas}} \\
w_g &= w + w_{s,gas} \\
w_{oil} &= w + w_{s,oil}
\end{aligned} \tag{2}$$

and are the equations examined in turbulence resolving calculations by Fabregat et al. (2015); 2016b).

A complete derivation of (2) is provided in the Appendix. The quantity $\boldsymbol{u} = (u, v, w)$ is a mixture velocity formed from the volume weighted average of the oil velocity $\boldsymbol{u_{oil}}$ and the seawater velocity $\boldsymbol{u_{water}}$. The quantities α_{oil}, α_{gas} and α_{water} are the volume fractions of oil, gas and water, respectively, T temperature, M_g is the mass of methane per unit volume and p is dynamic pressure. The quantities F^X are flux divergences of quantity X. All constituents are assumed to slip relative to the mixture at the (vertical) speed of $w_{s,\ X}$ where X is the relevant constituent. Oil and water are both taken as Boussinesq and their reference densities are assumed close enough that the mixture can also be considered as Boussinesq. Perhaps the most significant approximation is that gas is considered as dilute, i.e. that its concentrations are low enough that it does not significantly affect fluid volume. This appears explicitly in the volume fraction summation in (2). The buoyancy variable, B, includes explicit contributions from all phases as given in (3) below.

Inasmuch as we use solutions of (2) as references, we now discuss the sense in which these calculations are turbulence resolving. The model is based in the Spectral Element Method (SEM) code Nek5000 (Fischer et al., 2008b). Instead of explicit modelling of the subgrid terms using, for instance, a Smagorinsky eddy diffusivity (Özgökmen et al., 2009a; 2009b), we use the Spectral Vanishing Viscosity technique (Karamanos and Karniadakis, 2000) consisting of progressively filtering the near-grid scale coefficients in the spectral polynomial expansion (Fischer and Mullen, 2001; Deville et al., 2002). This approach is similar to increasing the nominal Reynolds and Péclet numbers only at the near-grid scales. Specifically, we used a 5% polynomial filtering of the two highest modes in the Legendre expansion for all the fields. With this, we ensure stability and preserve the exponential convergence of the solver while avoiding the computational cost associated with computing the sub-grid scale terms. Applications of this procedure to fully-developed, turbulent channel flows have shown excellent agreement with Direct Numerical Simulations (DNS), relative insensitivity to the filter specifics and overall computational efficiency (Koal et al., 2012). A turbulent spectrum for a rotating plume using this approach with resolution similar to that used in the present paper appears in Fabregat et al. (2016c).

There are two objectives for the remainder of this section. (1) First, we examine the general dynamics of a DwH-like plume with a particular interest in the impact of rotation on its development. For this purpose, we have conducted a turbulence resolving three dimensional simulation that due to computational overhead extends only for several hours. However, we argue that the importance of rotation is clear by that time. To more fully illustrate rotational effects, model solutions lasting several rotational periods (equivalent to several days of model time) are required. We are thus motivated to develop a computationally efficient two-dimensional version of the model representing the azimuthally averaged evolution of the system. This leads to our second objective, namely: (2) the assessment of our radially symmetric model relative to full three dimensional solutions. As shown below, radially symmetric models qualitatively capture purely thermal plume dynamics in the absence of rotation. In the presence of rotation, however, accurate 2d-3D comparisons in the purely thermal case require more careful tuning of RANS turbulence parameterizations. The inclusion of a slipping gas phase, independent of rotational effects, significantly erodes the quantitative accuracy of the 2d models.

2.1. A three-dimensional simulation

We have implemented (2) within the Nek-5000 model (Fischer et al., 2008a), a flexible Navier–Stokes equations solver using spectral elements. The flow configuration consists of a two-phase plume generated by a sustained injection of buoyant fluid and gas bubbles into a linearly stratified, motionless ambient. Oil is modelled as a light fluid without a slip velocity to reduce computational demands, while gas is a separate phase with its own constant slip velocity, $w_{s,\ gas}$. We have adopted $w_{s,gas} = 0.2$ m/s in agreement with Socolofsky et al. (2011) who, in turn, were motivated by Lehr et al. (2010). Gas slip velocity is determined largely by bubble size. Any DwH type release will result in a distribution of bubble sizes and thus a distribution of bubble slip velocities. The validity of using a single slip velocity (based on an average bubble size) to represent gas effects has been argued in Simiano (2005). While we adhere to this choice in the present manuscript, future plans call for investigating multiple gas slip velocities.

Mixture buoyancy is computed from

$$B = g\gamma(T - T_o)(1 - \alpha_{oil} - \alpha_{gas}) - g\frac{(M_g - \alpha_{gas}\rho_o) + (\rho_{oil}\alpha_{oil} - \alpha_{oil}\rho_o)}{\rho_o} \tag{3}$$

where γ is the thermal expansion coefficient of seawater, ρ_o a constant reference density midway between water and oil ($\rho_o \approx 900\,\mathrm{Kg/m^3}$), T_o a reference temperature and ρ_{oil} the density of oil. Pressure effects on the densities are not included. The mass of methane (M_g) in (3) will be neglected in the following for computational simplicity. Hence, the buoyancy force driving the plume is due to the lower density of the oil and gas phases and temperature effects on seawater density. The DwH inoculant entered the seawater at roughly 100 °C (Reddy et al., 2012) and entrainment of the ambient fluid, stratified in temperature, damps the buoyant plume anomaly. The inlet buoyancy flux B_o is

$$\begin{aligned}
B_0 &= w_0 AB(z=0) \\
&= gw_0 A\left(\gamma(T(z=0) - T_o)(1 - \alpha_{oil,o} - \alpha_{gas,o}) + \alpha_{g,o} + \alpha_{oil}\left(1 - \frac{\rho_{oil}}{\rho_o}\right)\right)
\end{aligned} \tag{4}$$

where the inlet is of cross-sectional area A. The notation X_o denotes the inlet value of X. Gas vents to the atmosphere at the slip velocity, but other materials obey a no-flux boundary condition.

An example 3d plume generated by our model appears in Fig. 1, where the parameters represent a DwH-like setting. A full analysis of this run appears in Fabregat et al. (2015), to which the reader is referred for further detail. Of relevance to this discussion, stratification was set to $N^2 = 2 \times 10^{-5}\ \mathrm{s^{-2}}$, and the net buoyancy flux was $0.4\ \mathrm{m^4 s^{-3}}$ (the net DwH flux was $1.4\ \mathrm{m^4 s^{-3}}$ where the buoyancy contributions from gas have been included). Fig. 1 is a snapshot of the turbulent plume 10 h after initiation. The grey shading represents the 'oil' in this simulation. The three main elements of the plume are: (i) its core from the base to the intrusion level, (ii) the intrusion, or spreading, level where the effective buoyancy anomaly of the plume has been erased by entrainment and (iii) the overshoot region above the intrusion level. The core of the plume widens from the wellhead via turbulent entrainment of the ambient. Part of the entrained cold ambient rises quickly enough that is it negatively buoyant at the spreading level. Above the intrusion, the bubbles keep rising because of their slip velocity. The introduction of the gas and the thermal anomaly over the wellhead creates a strong low pressure that draws deep fluid inwards towards the source (see Fig. 2). The inward directed mass flux results in

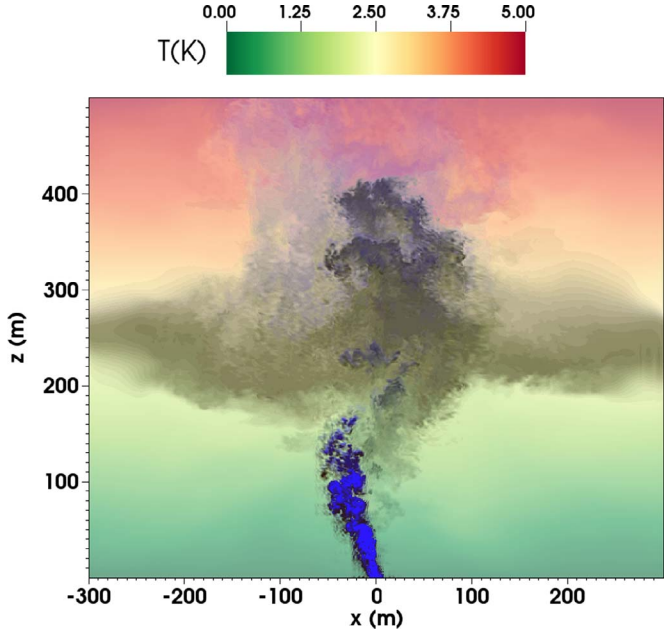

Fig. 1. Snapshot of the plume after 10 h. Blue is bubble concentration, gray is oil concentration and color is temperature difference from the bottom temperature.

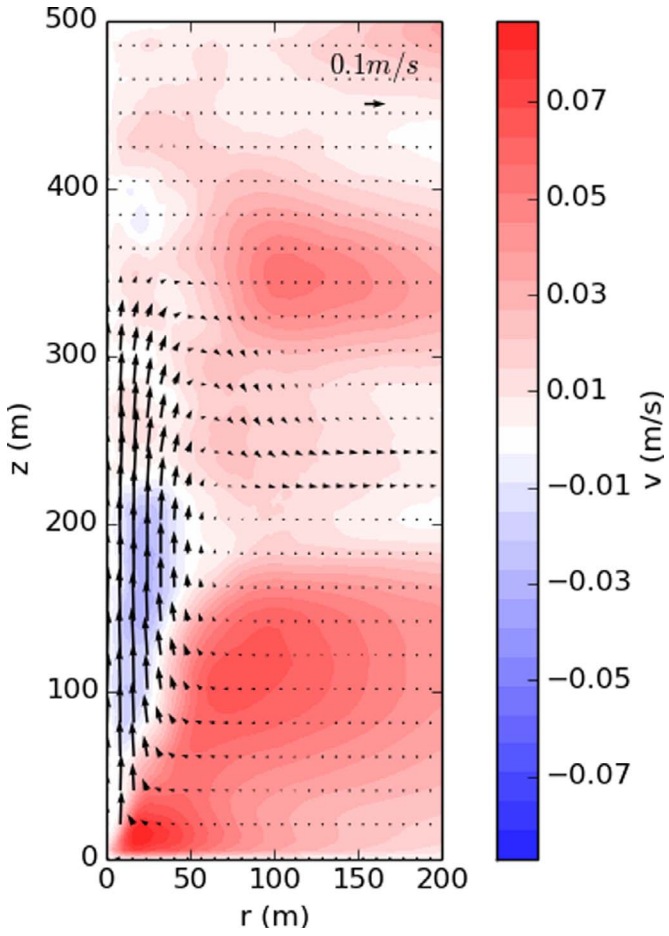

Fig. 2. Average radial and vertical velocity (shown as vectors) and azimuthal velocity (shown in color; blue is anticyclonic circulation, red is cyclonic). (For interpretation of the references to color in this figure legend, the reader is referred to the web version of this article.)

extreme vertical fluid velocities near the plume during its early evolution. These are generally in excess of 1 m s^{-1}, which greatly exceeds the model inlet velocity, and join with the bubble slip velocities to determine bubble motion.

The maximum rise height in Fig. 1 is roughly 250 m and large compared to the classical prediction of Morton et al. (1956)

$$h_T = 4.2 B_0^{1/4} N^{-3/4} \approx 194 \text{ m} \tag{5}$$

for a buoyant plume, where the multiplicative factor 4.2 has been calibrated from experiments. Given that the rotation period is roughly 18 h, the plume state at 10 h is not likely yet to be in equilibrium.

Rotation emerges as a surprisingly strong effect in this simulation, appearing primarily in the mean cyclonic swirl flows $O(0.1$ m/s) near the wellhead (Fig. 2). In non-rotating simulations, a swirl velocity failed to appear. The cause of the azimuthal flow can be traced to angular momentum conservation which results in a cyclonic flow as distant fluid is drawn to the source. We also find the instantaneous plume structure is generally not radially symmetric, and exhibits a precession around the well head. This appears in Fig. 1 in the slant of the plume away from the vertical. Time averaging the precession will lead to a radially symmetric average structure, however the final shape of the plume will be influenced by its presence.

The time scale for establishing a statistical steady state in a rotating system is related to the Coriolis parameter and thus typically a few rotation periods. Full three dimensional turbulence resolving Nek5000 integrations of this length for DwH parameters are currently too demanding to be practical (the computation in Fig. 1 required five days of wall clock time). This is a major motivation to examine 2d models, which are considerably more computationally economical. Of course, they require parameterization of the 3d plume turbulence and also suffer from an explicit exclusion of crossflows. Relative to the latter point, integral models which include crossflows often assume circular symmetry about the plume axis, so migrating lessons learned from 2d models to plumes in cross flows remains a possibility here. To address the question of parameterization, we have moved our 3d simulations from the DwH parameter setting to a parameter regime where computing for several rotation periods is more feasible. These then provide us with results to which we can calibrate the 2d model, as discussed in the next subsection. We generally have found turbulence parameterization in rotating plume settings is difficult, and is worsened with the inclusion of bubbles.

2.2. A radially symmetric model

Neglecting the non-vertical Coriolis parameter $\widetilde{f}$ and azimuthally averaging (2) returns an equation set that is azimuthally independent

$$\begin{aligned} \frac{\partial \boldsymbol{U}}{\partial t} + U\frac{\partial \boldsymbol{U}}{\partial r} + W\frac{\partial \boldsymbol{U}}{\partial z} + \frac{V}{r}\boldsymbol{k}\times\boldsymbol{U} + f\boldsymbol{k}\times\boldsymbol{U} &= -\nabla p + B\boldsymbol{k} + \boldsymbol{D}_{\boldsymbol{U}} \\ \frac{\partial \tau}{\partial t} + U\frac{\partial \tau}{\partial r} + W\frac{\partial \tau}{\partial z} &= D_\tau \\ \frac{\partial rU}{\partial r} + \frac{\partial rW}{\partial z} &= 0 \end{aligned} \tag{6}$$

The quantities $\boldsymbol{U} = (U,\ V,\ W)$ are the averaged radial (r), azimuthal and vertical (z) velocities, respectively. The quantity τ represents any of the tracers T, α_g or α_{oil}. Buoyancy B is defined in (3) and other notation is standard.

It should be noted that in an inviscid fluid, the azimuthal momentum equation reduces to Lagrangian conservation of angular momentum, λ

$$\lambda = rV + \frac{fr^2}{2} \tag{7}$$

Our mixture is not inviscid and thus not exactly conservative of angular momentum, but the behavior of the DwH model in Fig. 1 suggests angular momentum conservation strongly affects early plume

development.

The system (6) proved to be quite computationally economical. Computing several rotation periods with them required one day on a single processor, while comparable length calculations with the 3d model required roughly a week when run on ~ 800 processors.

The dissipative terms in Eqs. (6), where turbulence closures will be employed, represent the effects of the residuals emerging from the azimuthal averaging, i.e.

$$\begin{aligned} D_U &= \frac{1}{r}\frac{\partial r\overline{U'U'}}{\partial r} + \frac{\partial \overline{U'W'}}{\partial z} - \frac{\overline{V'V'}}{r} \\ D_V &= \frac{1}{r^2}\frac{\partial r^2\overline{U'V'}}{\partial r} + \frac{\partial \overline{V'W'}}{\partial z} \\ D_W &= \frac{1}{r}\frac{\partial r\overline{U'W'}}{\partial r} + \frac{\partial \overline{W'W'}}{\partial z} \\ D_\tau &= \frac{1}{r}\frac{\partial r\overline{U'\tau'}}{\partial r} + \frac{\partial \overline{W'\tau'}}{\partial z} \end{aligned} \tag{8}$$

where the primes denote the residuals and the overbar the averaging.

In the early plume models of Morton et al. (1956), radial profiles of all variables were assumed to be Gaussian, thus simplifying (6). Turbulence was parameterized using a simple entrainment hypothesis relating radially inward flow at the plume edge to the core plume vertical velocity. Here for the study of rotating systems we have elected not to employ this assumption. Rather, we adopted a Smagorinsky closure (Smagorinsky, 1963) for which the eddy viscosity coefficient ν becomes a function of the vorticity and strain in the flow field

$$\nu = l_s^2 S + \nu_0\,, \tag{9}$$

with ν_0 a background kinematic viscosity, and S the deformation given by

$$S^2 = 2\left[\left(\frac{\partial U}{\partial r}\right)^2 + \left(\frac{U}{r}\right)^2 + \left(\frac{\partial W}{\partial z}\right)^2\right] + \left(\frac{\partial U}{\partial z} + \frac{\partial W}{\partial r}\right)^2 + \left(\frac{\partial V}{\partial r} - \frac{V}{r}\right)^2 + \left(\frac{\partial V}{\partial z}\right)^2 \tag{10}$$

The quantity l_s is the Smagorinsky length scale that is adjusted to mimic the effect of unresolved non-axisymmetric eddies (Rotunno and Emanuel, 1987; Deremble, 2016). This parameterization automatically adjusts to the state of the flow, thus providing a spatially variable eddy viscosity coefficient. However, we have found this parameterization requires further tuning when applied to the present problem.

2.2.1. 2D-3D comparison

We have analyzed 4 different model deployments differing in rotation and the composition of the inlet buoyancy flux (either as a pure thermal buoyancy flux, or as a hybrid gas/thermal buoyancy flux). All other model parameters were common amongst the various simulations (see Table 1). The net buoyancy flux was the same for both the pure thermal and hybrid cases, and the rotating simulations were characterized by an effective Rossby number $Ro = N/f$. Stratification in the DwH region varied with depth, from a minimum of $N = 4 \times 10^{-4}$ s^{-1} to $N = 2.7 \times 10^{-3}$ s^{-1}, and the site was located at a latitude of roughly 28°N (Socolofsky et al., 2011). Thus the Rossby numbers ranged from $Ro \approx 11 - 40$. It should be noted that Rossby numbers in this range would normally lead to the neglect of rotation.

Very near the source, where we specify an outflow, the flow must resemble that of a jet rather than a plume (Hunt and Kaye, 2005). This is significant because jets entrain less than plumes. Defining α as an entrainment parameter, jets are characterized by $\alpha = 0.054$ while for plumes, $\alpha = 0.083$ (Turner, 1973). Numerous experiments performed with the 2d model revealed that the classical Smagorinsky scheme distorts this near well-head regime transition from the jet to the buoyant plume. The closure has a tendency to overmix very close to the well-head, and hence overentrain, at the base of the plume where the vorticity is the strongest. In contrast, this is where the entrainment coefficient should be the smallest. To capture this jet-plume transition, we have decreased the Smagorinsky coefficient near the well head, i.e. we multiply it by

$$\frac{1}{2}(1 + \tanh(15(z - L_m)))\,, \tag{11}$$

with L_m computed according to

$$L_m = 2^{-3/2}\alpha^{-1/2}M_o^{3/4}B_o^{-1/2} \tag{12}$$

The quantity L_m describes the transition height between momentum jet behavior and buoyant plume behavior (Hunt and Kaye, 2001) and for the parameters in Table 1, $L_m = 0.04$ m. The factor 15 allows to have a smooth transition in the Smagorinsky coefficient between the jet and the plume.

Table 1
Parameters for the 2d-3d comparison runs. The fourth column contains DwH parameters.

Parameter	Symbol	Value	DwH	Units
Inlet diameter	D	0.08	0.4	m
Slip velocity	w_s	0.016	0.20	m s^{-1}
Stratification	ζ	5.1	$\sim$ 0.004	K m^{-1}
Height of the domain	H	2.66	1500	m
Radius of the domain	R	2.66	∞	m
Gravity acceleration	g	9.8	9.8	m s^2
Inlet temperature	$T(z=0)$	12.7	100	C
Inlet gas volume fraction	$\alpha_{gas,\,0}$	0.00254	0.5	–
Inlet liquid phase velocity	w_0	0.04	2.0	m s^{-1}
Inlet buoyancy flux	B_0	5×10^{-6}	1.4	m^4 s^{-3}
Coriolis parameter	f	0.01	$\sim 0.4 \times 10^{-4}$	s^{-1}
Stratification frequency	N	0.1	$\sim 4 \times 10^{-4}$	s^{-1}
Reynolds number	Re	7071	$\sim 10^6$	–
Richardson number	Ri	3685	8.5×10^4	–
Péclet number	Pe	7071	$\sim 10^6$	–
Rossby number	Ro	10	$\sim$ 15	–

Several equilibrated plumes are compared in Figs. 3 and 4. The thermal plumes are denoted by $f_T = 1$ (left hand side) while hybrid plumes composed equally of thermal and gas components are denoted by $f_T = f_b = 0.5$ (right hand side). The top row are non-rotating cases and the bottom row are rotating examples.

The non-rotating thermal plume corresponds to a classic (Morton, 1957) case (see Fig. 3, upper left). The mean structure of the 3d model exhibits a 'classic' shape with intense vertical velocities at the center, an overshoot and a lateral penetration at the intrusion level appearing most clearly in radial velocity (Fig. 4, upper left). The 3d dynamics are well represented in a qualitative sense by the axisymmetric model with the modified version of the Smagorinsky parameterization. Maximum values for w are similar between 2d and 3d cases, as are their spatial distributions. In both the 2d and 3d cases, the plume exhibits an overshoot. The 3d radial velocity profile is reasonably well represented in the pure thermal case by the 2d model, even if the 2d outflow is a bit weaker. The maximum extent of the overshoot and the depth of the intrusion compare well. Comparable comparisons hold for the hybrid plume case.

Quantitative comparisons of centerline vertical velocity, temperature and gas volume fraction from the 2d and 3d non-rotating results appear in Fig. 5. Both non-rotating temperature and gas volume fraction are accurately portrayed by the non-rotating 2d results. Vertical velocity in the 2d model departs somewhat from that of the 3d profile very near the well-head. This is associated with the difficulties we have had tuning the Smagorinsky scheme very near the jet/plume transition zone. However, the overall structure of the thermal plume vertical velocity is well represented by the 2d model. Some degradation in the comparison appears for the hybrid plume.

The inclusion of rotation modifies the equilibrated plume considerably, even at this large Rossby number. Perhaps the most obvious

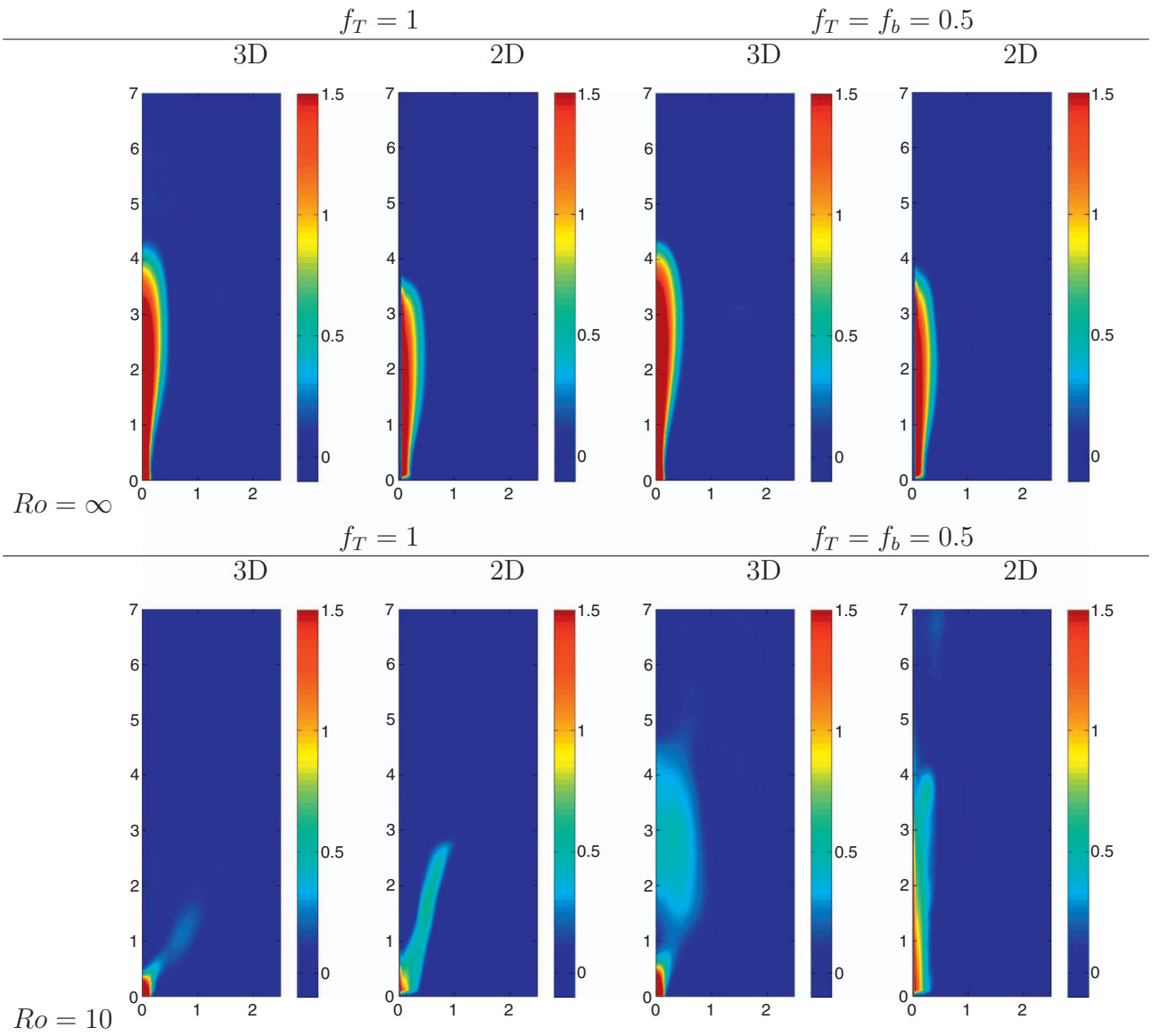

Fig. 3. Mean vertical velocity comparisons between 2d and 3d simulations. The left two panels are pure thermal plumes ($f_T = 1$) and the right two panels are hybrid plumes with one half of the buoyancy flux from thermal and bubble sources, respectively ($f_b = f_T = 0.5$). The upper panels are non-rotating ($Ro = \infty$) and the lower panels rotating ($Ro = 10$). Distances are non-dimensionalized by the scale 0.266 m. The velocities, shown in color, are non-dimensionalized by 0.0266 m/s.

effect is the weakening of the vertical velocities in the purely thermal case (see Fig. 3, lower left). In fact the plume penetrates sideways in the water column as indicated by the strong outward radial velocity (see Fig. 4, lower left). Plots of the 3d mean vertical velocity along the plume axis appear in Fig. 5 (top right) and serve to illustrate how strongly updrafts over the well-head are suppressed by rotation. By $z = 0.5$ (approximate two well-head diameters), vertical velocities for both rotating thermal and rotating hybrid plumes have effectively vanished. One must be approximately ten times further up the water column to find updrafts this weak in the non-rotating setting. The pure thermal plume even exhibits weak downdrafts on the centerline above $z = 1$. The vertical velocity from the 2d model also appears in this figure; it is discussed further below.

As shown in Fabregat et al. (2016a) and Deremble (2016), the weak vertical velocities and plume deflection are due to an adverse dynamical pressure gradient on the central axis which balances the buoyancy forces. By effectively pushing down on the wellhead, the pressure field prevents the direct ascension of the buoyant fluid. Instead, the fluid ejects from the wellhead region radially which severely reduces the plume vertical penetration along the central axis. The structure of the dynamical fields reflects the presence of rotation (Fabregat et al., 2016b).

To reproduce this in the 2d model of a rotating pure thermal plume, it was necessary to adjust the Smagorinsky parameterization yet again. Our most successful efforts, seen in Figs. 3 (bottom left) and 4 (bottom left), were obtained by returning to the basic Smagorinsky in (9) and eliminating the Smagorinsky viscosity acting on the swirl speed, leaving only the background viscosity. Other elements of the parameterization were left untouched. The very sharp swirl velocity front the 3d model develops near the wellhead, as a consequence of angular momentum conservation, generates very strong shears and strains that the pure Smagorinsky model overdamped. Without our adjustment, the 2d model failed to exhibit the off-axis updraft of the 3d results. With it, the spatial distributions of both the vertical and horizontal velocities in the purely thermal plume were represented well qualitatively, but the amplitudes were too strong. The 2d rotating thermal plume vertical velocity is compared to the 3d result in Fig. 5 upper right. The suppression of updrafting is evident and downdrafts on the centerline also

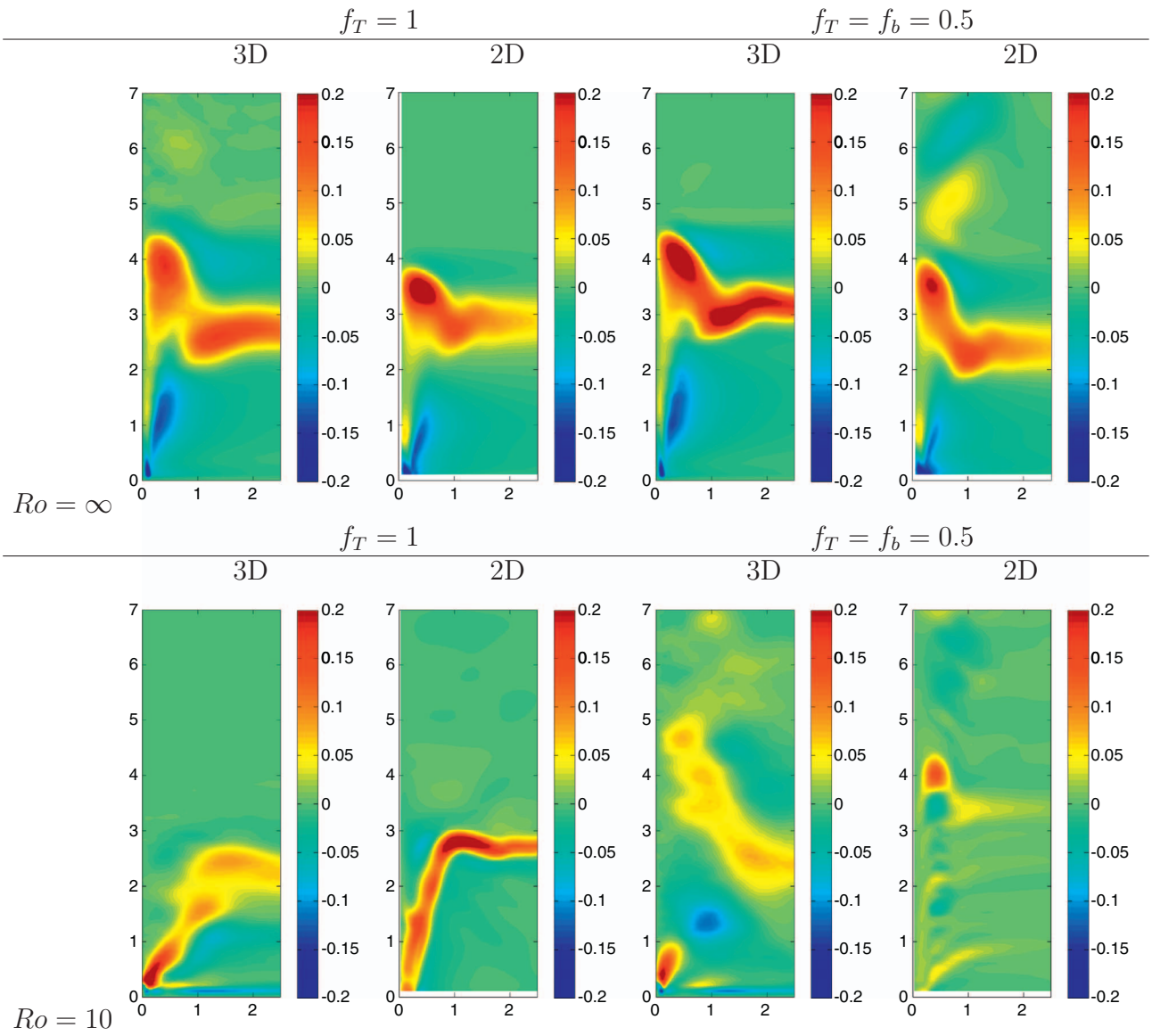

Fig. 4. Same as Fig. 3, but for radial velocity.

occur but are not as pronounced as in the 3d case.

Warm temperatures persist well up the axis in the non-rotating results for both cases but are largely confined to the well head area when rotation is included. Further up the column, the 3d temperature reverts to the background temperature for both rotating cases. This also appears in the 2d rotating thermal case, but the inclusion of bubbles yields 2d results departing noticeably from the 3d results.

The largest 3d gas fraction concentrations are near the wellhead in the rotating case; but then drop quickly in value to a nearly constant concentration (see Fig. 5). The non-rotating gas distribution penetrates much more effectively into the water column than for the rotating plume, but both converge to small values near the domain top because bubbles dominate the far field behavior for both cases.

The inclusion of bubbles degraded the 2d/3d comparison significantly for the rotating plumes. The bubble effect on the 3d simulation was strong, with the plume exhibiting upward directed flows everywhere along its central axis, in contrast to the pure thermal case. However, the amplitude of the updrafts was quite weak relative to the non-rotating case. This reduction of w was partly captured by the 2d hybrid model, but its spatial distribution was quite different. Downdrafts for the hybrid case outside of the main plume were seen in both the 2d/3d models around heights of $z \sim 3$ (see Fig. 3, lower right). Even with bubbles, the plume was directed off-axis, as seen in the radial velocities from the 3d run (Fig. 4, lower right). There are hints of off-axis structure in the 2d bubble run, but its signature in radial velocities was quite weak.

Quantitative comparisons between the 2d and 3d models in vertical velocity and mass flux appear in Fig. 6. Plots of the vertical velocity profile at $z = 3$ appear on the left for all four plume types. The 2d thermal plume is a bit weaker in vertical velocity than the 3d plume in the non-rotating cases, although the radial structure matches well, with downdrafts appearing off-axis. The 2d width matches the 3d with for the non-rotating thermal plume, but is a bit smaller for the non-rotating hybrid plume (zero crossing in vertical velocity of 0.5 for the 2d model, and 0.7 for the 3d model. A downdraft on the axis still exists at $z = 3$ for the 2d rotating model but is absent at $z = 3$ for the 3d case, reflecting the somewhat weaker suppression of the plume by the 2d model. The absence of any vertical flow at this depth occurs in both models beyond $r = 0.5$. The rotating hybrid plume vertical velocity at $z = 3$ compares somewhat better than would be expected from Fig. 3; the amplitudes and overall structure are well represented although the spatial distributions show discrepancies.

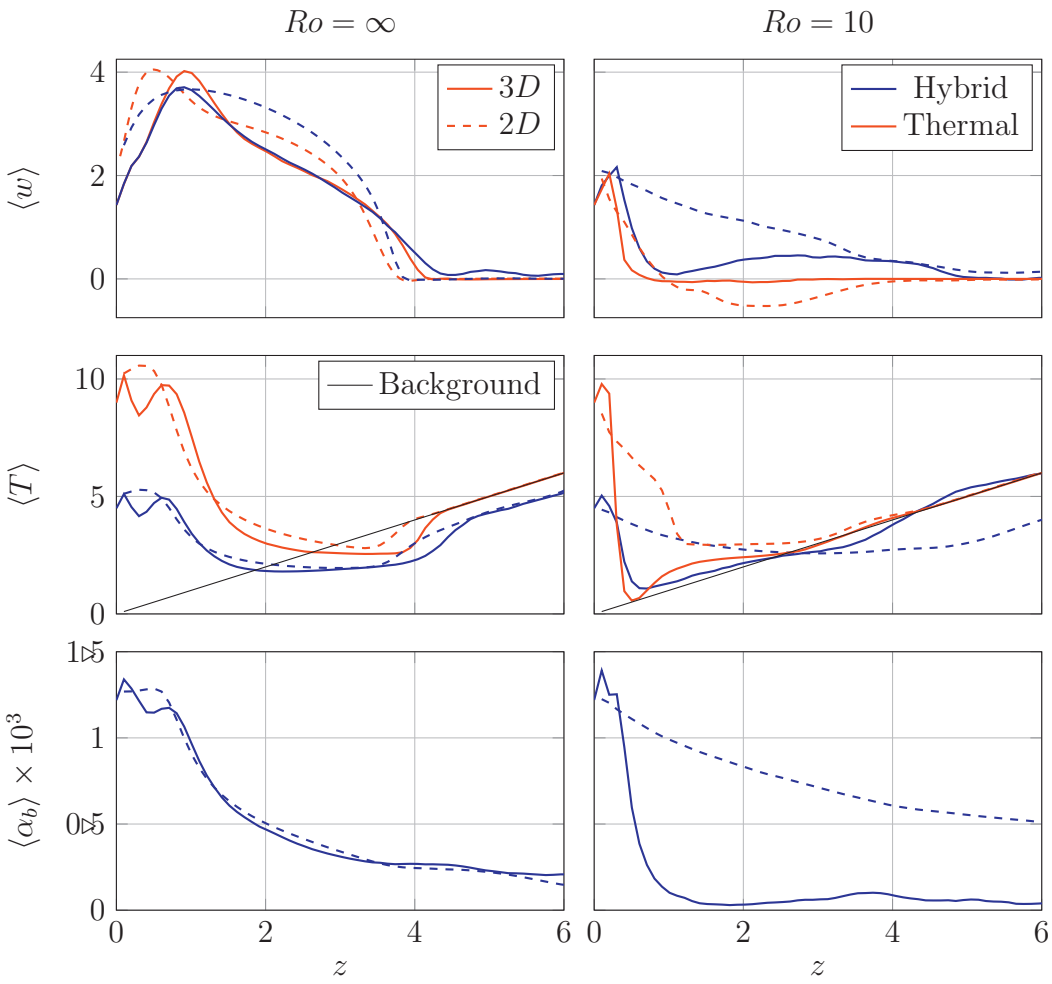

Fig. 5. Comparison of the vertical structure of mean centerline vertical velocity, temperature and gas volume fraction. $Ro = \infty$ (left) and $Ro = 10$ (right) with 3D results solid and 2D results dashed. Thermal plumes are in red and hybrid, thermal-bubble plumes in blue. (For interpretation of the references to color in this figure legend, the reader is referred to the web version of this article.)

The mass flux in the various models as a function of plume height appears on the right hand side. Similar statements can be made here as were made for vertical velocity. The non-rotating 2d model tends to underestimate flux in both updrafting and downdrafting zones but similar structure is seen. Broad updrafts and a weak downdraft are seen for both 2d and 3d rotating thermal plume calculations, but the spatial structure differ noticeably. The rotating hybrid case exhibits the least satisfactory comparisons. In summary, the 2d model captures much of the 3d results qualitatively. Quantitatively, the 2d model is overly weak compared to the 3d case but still agrees in magnitude for thermal and non-rotating hybrid plumes. The 2d hybrid plume model is poor in its ability to recover the 3d results.

We have met with some success when modeling 2-d non-rotating plumes with a modified Smagorinsky closure. Two dimensional rotating thermal plumes, with yet a different modified Smagorinsky closure, also exhibit the essential characteristics of the 3d solutions, although the quantitative comparisons clearly suffer. We have had no success with a 2d model of a hybrid rotating plume.

We identify several robust features of these simulations. First, rotation is a dominant effect in these large *Ro* simulations, where Ro is guided by field settings, and is responsible for establishing a cyclonic circulation in the wellhead near field during the early stages of plume development. The momentum is dominated by a cyclogeostrophic balance that blocks the inward directed mass flux, thus stifling the vertical velocity, even to the point that in a purely thermal plume it can be downward. This is quite distinct from the non-rotating system where strong, symmetric, upward convecting plumes always develop. The vertical flow suppression caused by rotation results in the buoyant fluid escaping laterally and at a slant from the wellhead. Our 2d results agree with the azimuthally averaged 3d results on this point, although as argued in Fabregat et al. (2015), the slant consists of a precession about the wellhead.

Last, there appears to be an effect of rotation on the turbulence near the wellhead. This is inferred from the need to strongly modify the Smagorinsky turbulence closure from that employed in non-rotating settings when finite Rossby numbers are studied. The importance of rotation is surprising because the Rossby numbers are so large that in classical geophysical fluid dynamics it would be ignored. The key is the geometry of the problem. The symmetry of the plume invokes angular momentum conservation in a radial framework which amplifies the rotational velocities of the background fluid as they draw toward the wellhead.

3. Application to a DwH-like event

Having assessed the 2d model, we exploit its computational efficiency to examine possible multiple rotation period plume structure for a DwH-like release. We proceed applying our 2d thermal plume model given the quantitative shortcomings of our 2d bubble plume model. Bubbles, however, clearly have a strong effect on the plume so these simulations can only comment qualitatively on the DwH plume.

The buoyancy flux in this case was set to 1.3 m^4/s^3, which compares

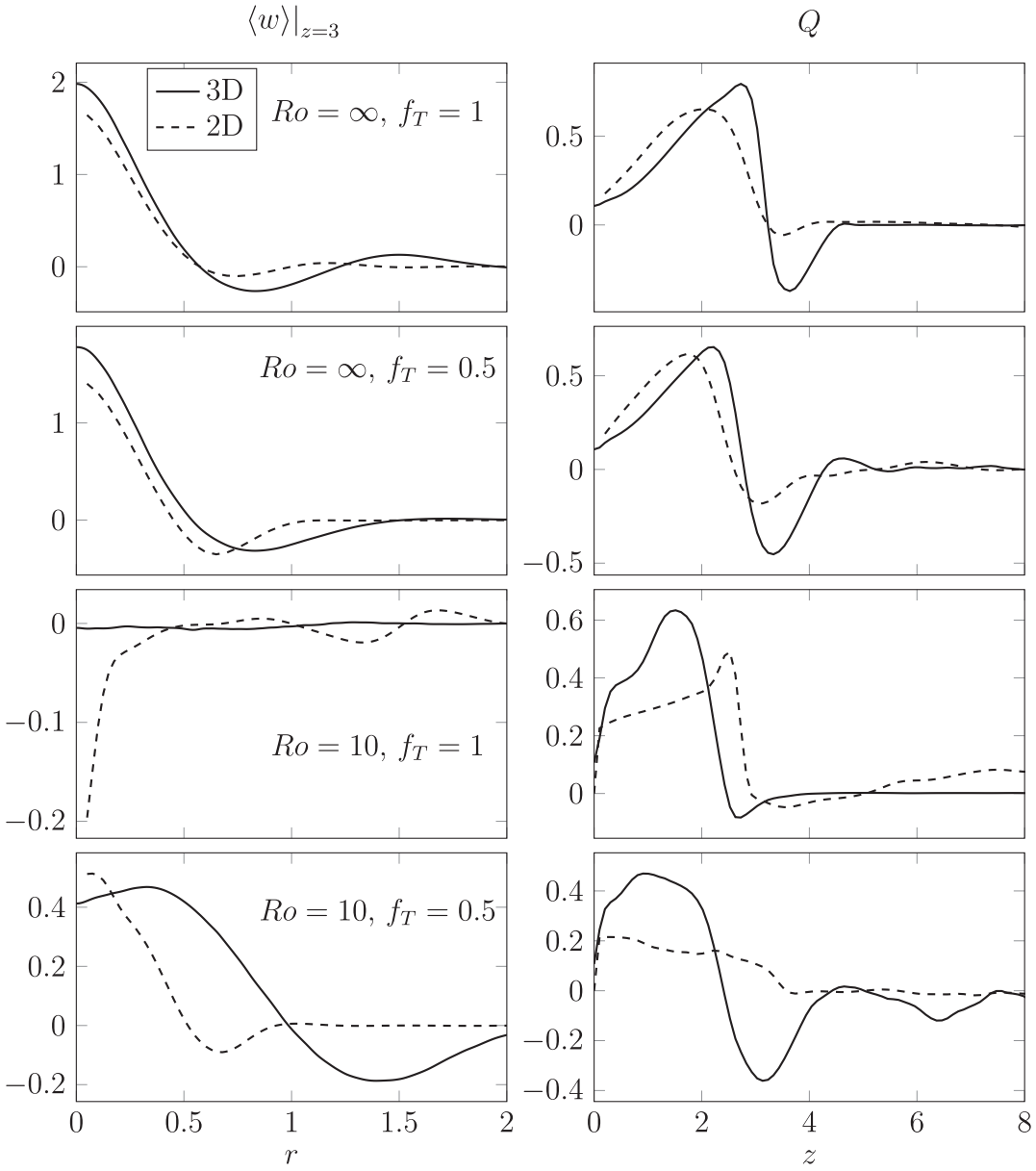

Fig. 6. Left: Radial profiles of the mean vertical velocity at $z = 3$ for the rotating and non-rotating thermal and hybrid plumes. Right: vertical profiles of the volume flux, Q. 3D results in solid lines, 2D results dashed.

well to the DwH value, including the gas effect. The domain lateral size is 1 km and its vertical dimension varied from 500 m to 1500 m depending on conditions. For comparative purposes, we compute a plume solution in the absence of rotation. When present, rotation was normally 10^{-4} s^{-1} and the two buoyancy frequencies $N^2 = 10^{-6}$ s^{-2} and $N^2 = 2 \times 10^{-5}$ s^{-2} were studied, the former being more representative of the DwH site. The resulting Rossby numbers, $N/f = 10, 45$ respectively, bracket that of the DwH site. We also examined the unrealistic rotation rate $f = 4.5 \times 10^{-4}$ s^{-1} in conjunction with the stronger stratification in order to study strong rotation in a more stratified setting.

Swirl velocity at the edge of the well head and the vertical velocity at the plume center were monitored until their time series stabilized (about 2 days, or 3 rotation periods, for both Rossby numbers). The simulations proceeded out to 10 days (14 rotation periods), without major changes after 2 days in the structure of the fields. Longer periods were not studied because the DwH site was affected by time dependent background flows, and that periods of relative calm, in which one might anticipate a purely 2d model would be useful, were unlikely to last beyond a few days. We focus here on the eventual steady (or statistically steady) states reached by the 2d model.

Fig. 7 compares the steady states for $Ro = \infty$, 45 and 10 for the DwH-like settings. The last of these is perhaps the most 'realistic' with regards to the DwH event itself in that the stratification $N = 10^{-3}$ s^{-1} is representative of the area (recall DwH occurred in 1500 m of water). Note also the vertical scale for the third setting (to 1500 m) differs from the prior two. Streamfunction appears on the left and the distribution of a passive scalar on the right. All plots are from 5 days.

The non-rotating plume takes on a very classic structure of an overshoot and plunge near plume center, followed by a spreading layer. The (Morton et al., 1956) spreading layer depth scaling

$$h_T \sim 3.1 \frac{B_o^{1/4}}{N^{3/4}} = \frac{(1.3\ \text{m}^4\text{s}^{-3})^{1/4}}{(4.5 \times 10^{-3}\ \text{s}^{-1})^{3/4}} = 190\ \text{m} \tag{13}$$

describes the numerical spreading depth quite accurately. The passive scalar tracks an extended spread out to a distance of at least 1 km. The inclusion of very weak rotation ($R_o = 45$, Fig. 7, middle) modifies the picture significantly. The previously described outward slant appears with indications of downdrafts very close to the plume axis. The

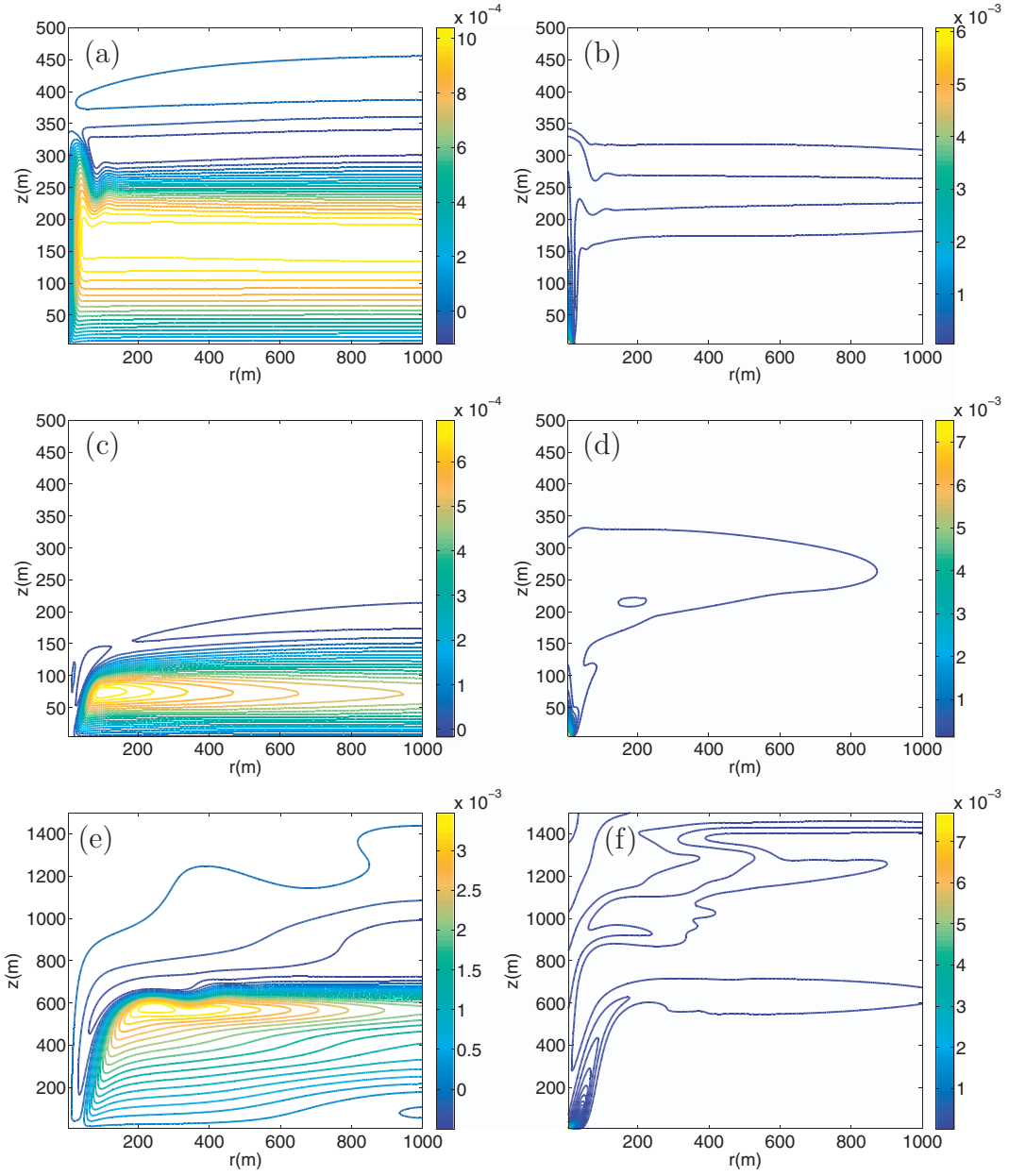

Fig. 7. Streamfunction (left) and passive scalar (right) at $Ro = \infty$ ($N = 4.5 \times 10^{-3}$ s^{-1} and $f = 0$) (top), $Ro = 45$ ($N = 4.5 \times 10^{-3}$ s^{-1} and $f = 10^{-4}$ s^{-1}) (middle) and $Ro = 10$ ($N = 10^{-3}$ s^{-1} and $f = 10^{-4}$ s^{-1}) (bottom) at $t = 5$ days.

spreading layer depth is strongly depressed, here achieving a height of approximately 125 m, i.e. roughly 60% of that noted in the non-rotating case. There is evidence of a spreading layer at a height of 250 m in the passive scalar, but this is a remnant of the initial adjustment process. Very early in the rotating evolution, the plume penetrates to heights comparable to those of the non-rotating case. With the development of the swirl velocity, the plume moves off-axis and retreats to its final spreading height seen in Fig. 7, where it remains to at least 10 days. Later plots (not shown) indicate an active spreading layer at 125 m and an inactive remnant at 250 m.

To move the rotating case more clearly into the DwH regime, the stratification was reduced to $N = 10^{-3}$ s^{-1}, the results of which appear in Fig. 7, bottom panel. Once again, the off-axis plume appears and clear indications of downdrafts are seen on the plume axis. With the reduced stratification, plume penetration is much more effective, now reaching a height of roughly 600 m. The active spreading layer is clearly well developed at 600 m and a remnant of the initial plume development appears around 1300 m. The (Morton et al., 1956) scaling for the maximum plume height predicts

$$h_T \sim 4\frac{B_o^{1/4}}{N^{3/4}} = \frac{(1.3\ \mathrm{m^4 s^{-3}})^{1/4}}{(10^{-3}\ \mathrm{s^{-1}})^{3/4}} = 760\ \mathrm{m} \tag{14}$$

The addition of strong rotation suppresses the plume spreading level at 5 days by roughly 160 m. It was noted above for weaker rotation the total suppression was about 65 m (190 m–125 m). Increasing the strength of the rotation by a factor of 4 results in a greater plume suppression, although the effect is not linear in the Rossby number. A separate interesting result of this experiment (not shown here) is that the plume slowly grows in height for the next several days. This has the effect of broadening the width of the actively spreading plume. What is a roughly 100 m thick spreading layer centered at 600 at day 5 becomes a roughly 200 m thick layer centered at 750 m by day 10. These results argue the system is not yet fully equilibrated. We do not explore this further however, because these experiments are constrained by the lack of other likely more important variability sources, like background

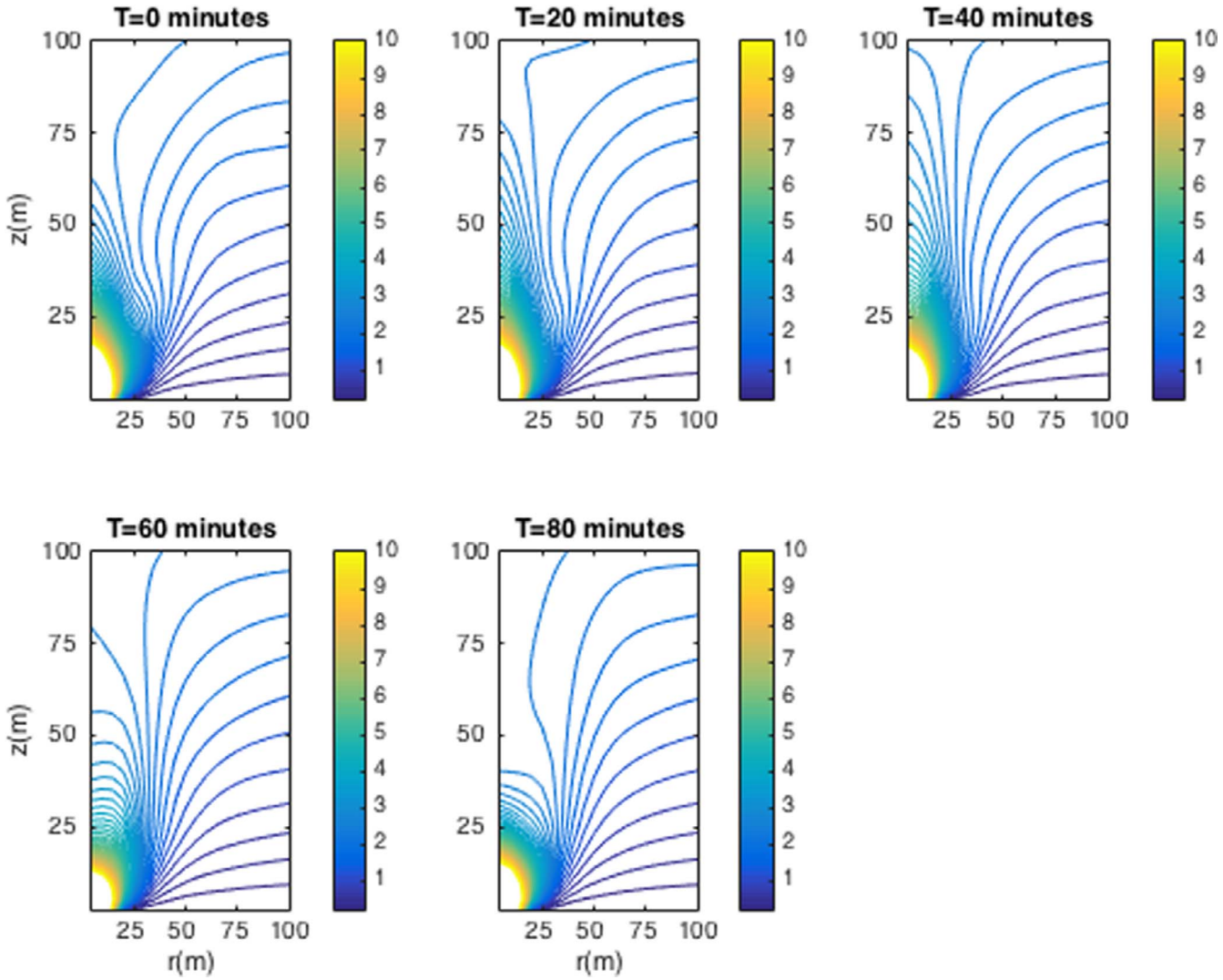

Fig. 8. The structure of the strongly stratified and strongly rotating plume oscillation as it appears in temperature. Twenty minutes separates each plot.

flow.

To broaden our parameter regime, we also considered a strongly rotating plume in a strongly stratified setting, using $N = 4.5 \times 10^{-3}$ s^{-1} and the unrealistic Coriolis parameter $f = 4.5 \times 10^{-4}$ s^{-1}, which yields a Rossby number of 10. The early plume evolution for this case resembled that of both previous simulations, showing a rapid development of plume penetration followed by a slower retreat of the plume towards an eventual roughly equilibrated depth of 130 m. However, the most unexpected finding from the simulation was the plume did not settle into a steady state. Rather, the depth of maximum plume penetration cycled between two depths approximately 130 m apart, from a maximum of 200 m to a minimum of 75 m. The oscillation as illustrated in temperature at 20 min intervals appears in Fig. 8 and in angular momentum in Fig. 9. It consists of periodic increases and decreases in the height of plume penetration, visible in temperature, and on and off-axis plume excursions, visible in angular momentum. The angular momentum surfaces also show wave like propagation away from the plume, consistent with gravity wave dynamics. The oscillation period is roughly 1.5 h, which is easily supported as a gravity wave by the stratification (buoyancy period $\sim$ 20 min). It is interesting that even though rotation is strengthened by a factor of 4 relative to the strongly stratified results appearing in Fig. 7 middle, the mean plume penetration depth is not much different between them. This reflects the continuing transition of the transient plume between a relative efficiently penetrating on-axis plume state and a suppressed and poorly penetrating off-axis plume state. This both slows and thickens the spread of the passive scalar. As seen in the bottom right plot in Fig. 9, at 5 days, the passive tracer is several hundred meters thick and has spread only to 600m.

Deremble (2016) in an exploration of the steady solutions of the 2d model equations found regimes of multiple equilibria characterized in his case by an on-axis solution and an off-axis solution. Both solutions were stable for the parameter settings he explored. It is thus possible, if speculative, that for DwH parameters, multiple steady solutions of the equations exist, but are unstable. In this case, the oscillation would represent the repeated approach of the system to one of those unstable states followed by its repulsion to another unstable state.

4. Discussion

We have here introduced and tested a multi-phase model designed for use in the deep ocean. We are motivated by the recent Deepwater Horizon event and the continuing exploration for oil in the ocean. The aims of the derivation were to retain the essential elements of the problem while simplifying the model as possible for economy in computations.

We have derived an Eulerian model to more easily interface with ocean general circulation models, and it is effectively Boussinesq, in that both oil and water are treated as individually and jointly Boussinesq. The equations, derived in discrete form using an integral approach, make clear the need for inter-volume exchange

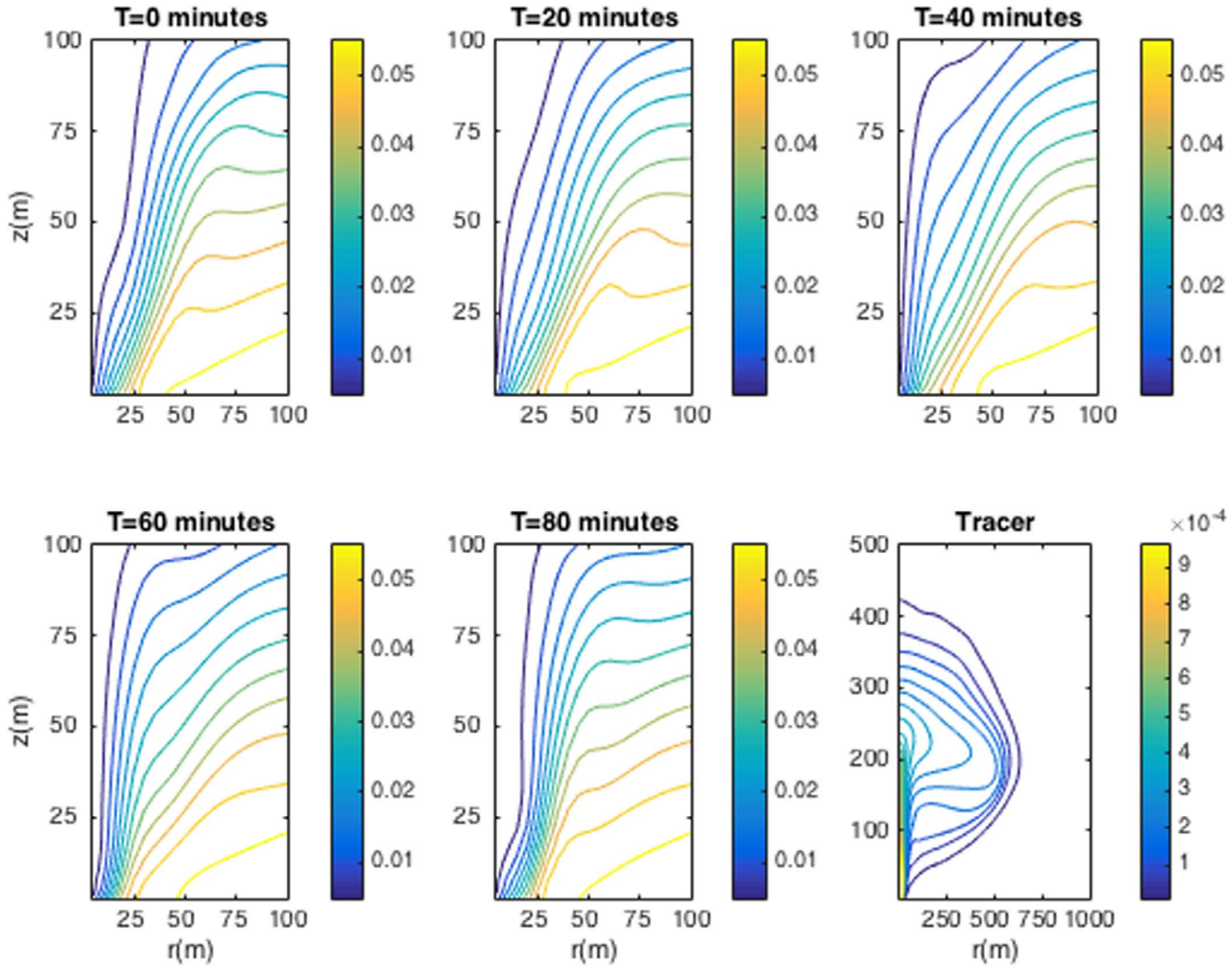

Fig. 9. As Fig. 8, but for angular momentum, which is approximately a materially conserved quantity. The bottom right plot is of a passive tracer at day 5.

parameterizations. With relatively intuitive choices for these parameterizations, the equations correspond to the discrete representation of an underlying set of partial differential equations.

We have calibrated and applied the model to DwH-like buoyant convection problems to develop intuition about the relevant fluid mechanics and plume behaviors. The 2d model works best for purely thermal plumes without bubbles; rotating bubble plumes have not yet been satisfactorily modeled using our 2d approach. Perhaps the greatest surprise in the solutions is the importance of rotation to the eventual statistical steady state. This tends to more effectively trap fluid in the vicinity of the wellhead and nurtures the development of near field swirl speeds. Rotational plumes exhibit a strong tendency to ascend upward off the plume central axis and can show downward velocities over the wellhead.

It has proven surprisingly difficult to develop a 2d model that compares well to our 3d results, both in non-rotating and rotating settings. We have tried several different closure schemes before settling on a modified Smagorinsky model. The main difficulty appeared to be capturing the very near well-head transition from a constant volume flux jet to a thermal plume, a location where the classical Smagorinsky algorithm induced overly strong mixing, and hence entrainment, relative to the 3d results. We were able to overcome this issue by weaking the Smagorinsky formulation near the well-head for the non-rotating case. This prescription, however, did not work when rotation was introduced, and we eventually employed a Smagorinsky closure to all variables except the swirl speed. We were able to capture the off-axis spread of the rotating plume in this way. We believe the lesson learned here is that the nature of the turbulence at the well-head is influenced by rotation, even at these relatively large Rossby numbers. We were also unable to produce an acceptable 2d model of a hybrid plume.

The picture emerging from these studies differs from the classical non-rotating plume models that have been applied to the DwH event (Socolofsky et al., 2011) and the question arises if the observations support one model type over the other. What is most clear from the data is that a reasonably well-defined plume of low oxygen and high fluorescence, consistent with exposure to Macondo hydrocarbon, was found at roughly 1175 m depth, some 350 m above the wellhead, and streamed primarily to the southwest from the release site (Camilli et al., 2010; McNutt et al., 2012; Reddy et al., 2012; Spier et al., 2013). The thickness of the plume was between 100 and 200 m and high hydrocarbon concentrations were observed over a potential density range of 0.06 kg/m^3 (Socolofsky et al., 2011). At least three other shallower depths also exhibited evidences of plumes, but we focus on the deepest one due to our interests in nearfield plume development. Trapping depths like this have been predicted from the non-rotating models (Socolofsky et al., 2011), however, it is also possible to infer such behavior from the results reported here. We have computed spreading heights from 130 m to 600 m depending on the stratification. These heights emerge from our pure thermal plume, however trapping heights like this have also been seen in our 3d DwH-like simulations. There is

also some suggestion of intrinsic variability in the rotating plumes. Whether the same occurs for the non-rotating plumes is unclear, although it has not appeared in any of our computations. Intrinsic plume penetration variability thus emerges as a possible contributor to the width both in physical space and in density space of the high hydrocarbon observations.

The biggest distinctions in the structures of the rotating and non-rotating plumes occur in the velocity fields around the plumes. Specifically, swirl velocities are absent from the non-rotating plumes and the rotating plumes are much broader in near field diameter.

There are few observations that can comment on these details. Camilli et al. (2012) report DwH plume velocity measurements within meters of the wellhead, but these are focussed on vertical velocities, are only a few minutes in duration and were taken in the transition between the failed 'Top Fill' confinement exercise and the commencement of the 'Top Hat #4' placement. At that point, the release was confined to a single leak by severing the connection to the open end 'Riser' about 250 m from the DwH wellhead. It is unclear how to interpret the results presented here in terms of these measurements but it does seem the data mentioned above cannot discriminate between the predictions of the non-rotating models and our rotating results.

One other interesting observational result also bears explicit mention. In an analysis of all available quality controlled NOAA and BP hydrocarbon data, Spier et al. (2013) found that the surface oil expression above the release site was roughly 1.6 km in diameter, and thus considerably broader than the 0.3 km diameter surface footprint predicted by the non-rotating models. Lateral enhancement of the near-field plume is a natural result of the rotational dynamics in our model; a simple updrafting over the wellhead at a spreading angle of roughly 0.1 is prevented by the adverse vertical pressure gradient. Instead, the buoyant fluid is forced to escape laterally and spreads much more effectively in the near field. As opposed to the non-rotating plume radii of $\sim$ 50 m at the spreading level, we routinely see plume radii in excess of 250 m at the spreading level (see Fig. 7).

4.1. Future work

While the literature supports the use of a single gas slip velocity to capture the multiphase nature of a bubble plume, our model allows the inclusion of more than one bubble size, and hence more than one slip velocity. Numerical simulations are underway to examine the impact of this modification.

However, the most important factor not yet explored for rotating multiphase plume is undoubtedly crossflow. The scale estimates presented in Socolofsky et al. (2011) suggest the DwH event was more 'stratification' dominated than 'cross-flow' dominated. It remains to determine how to distinguish between these two regimes for the case of rotating buoyant point source releases. Our plans are to pursue such simulations, although this promises to be a computationally demanding problem because of the need move beyond the economical 2d model and compute multiphase behaviors over a much larger area. However, it is possible that lessons from the symmetric simulations can be imported to the cross-flow problem in the manner that they have been for non-rotating plumes (Zheng et al., 2003).

Acknowledgments

This research was made possible by a grant from The Gulf of Mexico Research Initiative. Data are publicly available through the Gulf of Mexico Research Initiative Information & Data Cooperative (GRIIDC) at https://data.gulfresearchinitiative.org (doi:R4.x265.000:0023). Much of the initial work was done during a visit by one of us (WKD) to CUNY-SI, for which the hosts (AP, AF) and host institution are gratefully thanked. The present manuscript was aided greatly by two thorough, anonymous reviewers.

Appendix A. A multiphase model for Deepwater oil spills

Multiphase flows are well known in the engineering community, but less so among oceanographers. We therefore present here a development of the equations for two phases of liquid and one phase of gas along with a discussion of the errors and approximations.

The equations governing each phase of the mixture are the stratified Navier–Stokes equations, consisting of mass, momentum and energy equations, along with tracer equations related to fluid or gas density by an equation of state.

The momentum equations are

$$\frac{\partial}{\partial t}(\rho_i \boldsymbol{u}_i) + \nabla\cdot(\rho_i \boldsymbol{u}_i \boldsymbol{u}_i) + \boldsymbol{f}\times\rho_i\boldsymbol{u}_i + \nabla\pi_i + \nabla\cdot\mathbb{F}_i^{(x)} = 0 \tag{A.1}$$

where the subscript i denotes a particular mixture constituent, π_i denotes pressure and $\mathbb{F}_i^{(k)}$ denotes the viscous fluxes in the k direction. The quantities $f = 2\Omega\sin\theta, \widetilde{f} = 2\Omega\cos\theta$ are the Coriolis parameters with the former the more familiar, vertical one, and other notation is standard. We keep both Coriolis components in view of the relatively weak stratification of the deep ocean and the recognized effects of full rotation on convection in the mid and equatorial latitudes (Sheremet, 2004). The mass equations can be written as

$$\rho_{it} + \nabla\cdot(\rho_i \boldsymbol{u}_i) = 0 \tag{A.2}$$

where we ignore biological and chemical degradation of oil and gas, and the tracer equations as

$$(\rho_i T_i)_t + \nabla\cdot(\rho_i \boldsymbol{u}_i T_i) + \nabla\cdot\boldsymbol{F}_{Ti} = 0\,, \tag{A.3}$$

where $\boldsymbol{F}_{Ti}$ represents the diffusive flux of property T_i. Tracers and density are linked via equations of state of the form

$$\rho_i = \rho_i(T_i, p_i)\,, \tag{A.4}$$

where there can be more than one tracer, T_i, involved in the equation of state (e.g., temperature and salinity for seawater).

All of the prognostic equations involve a so-called 'conservative' operator of the form

$$\mathbb{Z}(p_i) = (\rho_i p_i)_t + \nabla\boldsymbol{\Psi}_{Pi}\,, \tag{A.5}$$

where $\boldsymbol{\Psi}_{Pi}$ is a generalized flux of property p_i. For example, the generalized flux of the tracer T_i is

$$\boldsymbol{\Psi}_{Ti} = \boldsymbol{u}\rho_i T_i + \boldsymbol{F}_{Ti} \tag{A.6}$$

and consists of both advective and non-advective parts.

The equations governing the evolution of constituent i do not apply everywhere in space. Rather, they are limited in their influence to domains where constituent i is found; interactions between the constituents occur at interfaces that separate the various constituent domains. To write

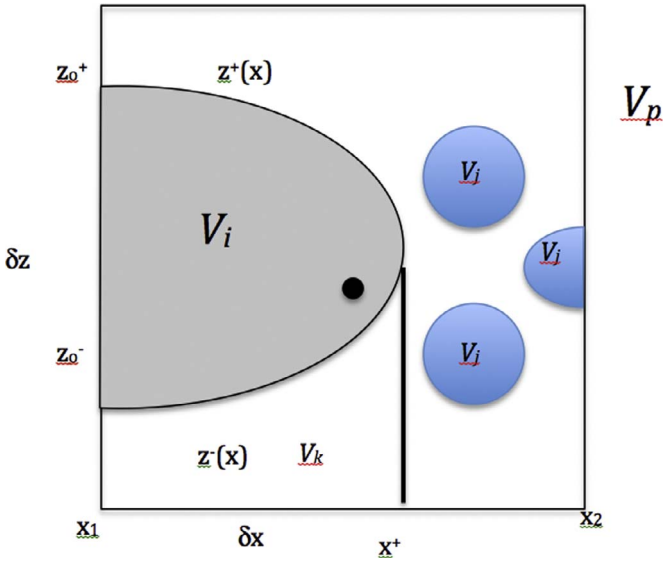

Fig. A.10. Two-dimensional grid schematic with three constituents denoted by *i*, *j*, and *k*. The east-west (δx) and vertical (δz) dimensions of the cell are shown and the center domain point is indicated by the large dark dot. The shaded area is the sub-domain of constituent *i* (V_i), the blue areas are constituent *j* and both are embedded within a cell otherwise full of constituent *k*. The full square is the domain V_p over which the integration is carried out. The interior interfaces between constituents *i* and *k* are denoted by $z^+(x)$ and $z^-(x)$ and extends from the fixed grid boundary at $x = x_1$ to the interior point x^+. The intersections of the grey interface with the grid boundary are denoted by z_o^- and z_o^+. (For interpretation of the references to color in this figure legend, the reader is referred to the web version of this article.)

globally valid equations then, it is necessary to multiply each of the above equations by a variant of the Heaviside step function, here denoted by $H_i(\boldsymbol{x})$, ($H_i(\boldsymbol{x}) = 1$ if constituent *i* is found at location; $H_i(\boldsymbol{x}) = 0$ otherwise) and sum them. Thus, for example, the general form of the east west momentum equation becomes

$$\sum_i H_i[(\rho_i u_i)_t + \nabla(\rho_i \boldsymbol{u}_i u_i) - f\rho_i v_i + \widetilde{f}\,\rho_i w_i + \pi_{ix} + \nabla \mathbb{F}_i^{(x)}] = 0 \tag{A.7}$$

which is valid at every point in space.

We now apply an integral approach where the general equations will be integrated over a fixed volume and budgets for each of the properties developed. A helpful first demonstration of this procedure follows from volume integrating the conservative operator in (A.5)

$$I_p = \int_{V_p} \left[\sum_i H_i[(\rho_i p_i)_t + \nabla \boldsymbol{\Psi}_{Pi}] \right] dV = \sum_i \int_{V_i} [H_i[(\rho_i p_i)_t + \nabla \boldsymbol{\Psi}_{Pi}]] dV_i \,. \tag{A.8}$$

In the first integration, the quantity V_p denotes a volume centered on a fixed location where we wish to know how a bulk dynamic quantity *p* (e.g., volume averaged density or momentum) will evolve. On the right hand side of (A.8), the volumes V_i are restricted to the regions inhabited by constituent *i* inside V_p. The surfaces bounding V_i are of two types. They are either interfaces within the larger volume V_p, or they are surfaces on the bounding faces of V_p wholly encircled by an interface separating *i* from some other constituent (a two dimensional example appears in Fig. A.10). The behaviors of these two surfaces are fundamentally different, with the former free to move within V_p and the latter constrained to lie on a surface fixed in space.

For a two-dimensional case, (A.8) becomes

$$\int_{x_0}^{x_1} \int_{z_0}^{z_1} \left[\sum_i H_i[(\rho_i p_i)_t + (\Psi_{pi})_x + (\Psi_{pi})_z] \right] dz dx = \sum_i \int_{x_0}^{x_+} \int_{z_-}^{z_+} [(\rho_i p_i)_t + (\Psi_{pi})_x + (\Psi_{pi})_z] dz dx \tag{A.9}$$

and consider the single integral over constituent *i* (shown as grey in Fig. A.10). The last integral is trivial to perform. Pulling the derivatives out of the integrations in the first two right hand side terms and recalling that the interface inside V_p can move returns

$$I_{p_i} = \frac{d}{dt} \int_{x_o}^{x_+} \int_{z_-}^{z_+} \rho_i p_i dz dx + \underline{\int_{x_0}^{x_+} (\rho_i p_i z_t^+ - \boldsymbol{\Psi}_{p_i} \cdot (\boldsymbol{k} - z_x^+ \boldsymbol{i}))dx} - \underline{\int_{x_0}^{x_+} (\rho_i p_i z_t^- - \boldsymbol{\Psi}_{p_i} \cdot (\boldsymbol{k} - z_x^- \boldsymbol{i}))dx} + \int_{z_o^-}^{z_o^+} \boldsymbol{\Psi}_{p_i} dz \tag{A.10}$$

The underlined terms vanish upon the summation because they represent exchanges entirely within V_p. For example, if $p = 1$ (we consider mass), the underlined terms take the form

$$\int_{x_0}^{x_+} \rho_i (z_t^+ - u_i z_i x + wi) dx = 0 \,, \tag{A.11}$$

which vanishes due to the immiscibility of the fluids. A similar result holds for all properties, *p*. The remaining non-advective fluxes are due to viscous or diffusive effects. These are incapable of producing momentum, mass or heat (neglecting the viscous heat of dissipation) and so will simply redistribute these properties between constituents within the fixed volume. Thus the intuitively pleasing result is found that the bulk change of property *p* within the volume element caused by conservative processes is wholly controlled by the generalized multiphase flux of *p* through the fixed boundaries of the domain

$$\sum_i I_{pi} = \sum_i \left[\frac{d}{dt} \int_{V_i} \rho_i p_i dA_i + \oint_{\partial V_{pi}} \boldsymbol{\Psi}_{pi} \cdot \boldsymbol{n}_p dl_i \right]. \tag{A.12}$$

This argument is easily generalized to three dimensions.

An analogous procedure can be applied to the pressure gradients in the momentum equations. In principle the pressures across interfaces can differ due to processes like surface tension. For the present oceanographic application these will be ignored. Applying continuity of pressure at interfaces within V_p thus yields

$$\sum_i \int_{V_i} \nabla p_i dV_i = \int_{S_p} p \boldsymbol{n} dS_p \,, \tag{A.13}$$

where the continuity of pressure has allowed the removal of the constituent subscript.

The only remaining momentum quantities are the Coriolis accelerations, which are straightforward to integrate, thus completing the volume-based discretization of (A.1). To this point, the only approximations that have been made are the neglect of surface physics associated with the contact between the fluid constituents at their interfaces.

We now introduce the more important approximations. Consider first the form of the integrated mass equation

$$\frac{d}{dt} \sum_i \int_{V_{pi}} \rho_i dV_i + \sum_i \int_{S_i} \rho_i \boldsymbol{u}_i \cdot \boldsymbol{n} dS_i = 0 \,. \tag{A.14}$$

The net mass in the mass control volume has contributions from oil(s), water and gas(es), the densities of which are greatly different. Water density is roughly 1035 kg m^{-3} in the deep ocean, oil is at most about 840 kg m^{-3} and at 150 atmospheres, methane is roughly 100 kg m^{-3}. If we adopt a density scale of

$$\rho_0 = \frac{\rho_{oil} + \rho_{water}}{2} = 937 \text{ kg m}^{-3} \tag{A.15}$$

water and oil density variability relative to ρ_0 is about 10%, while the full gas density is only about 10% of ρ_0. Often in such models, the bubble mass is neglected, i.e. the bubbles are modelled as 'voids'. We adopt this approximation. Considering the extreme case of a volume of half gas and half oil, the volume average density is 460 kg m^{-3}, as compared to the approximate density estimate of 425 kg m^{-3} obtained by entirely neglecting the gas. The error, more than 10% here, will be smaller for other less extreme settings. Neglecting gas density, the mass equation becomes

$$\frac{d}{dt} \sum_{i \neq i_g} \int_{V_{pi}} \rho_i dV_i + \sum_{i \neq i_g} \int_{S_{pi}} \rho_i \boldsymbol{u}_i \cdot \boldsymbol{n} dS_i = 0 \tag{A.16}$$

where i_g denotes indices reserved for gases. To simplify (A.16) further, we write

$$\int_{V_{pi}} \rho_i dV_i = \overline{\rho_i} \delta V_i; \quad \int_{S_{pi}} \rho_i \boldsymbol{u}_i \cdot \boldsymbol{n} dS_i = \overline{\boldsymbol{u}_i \rho_i} \delta S_i \,, \tag{A.17}$$

where the overbar denotes either a volume average over the constituent volume or a surface average over a constituent surface on the cell volume boundary. Which definition applies will be clear by context. Dividing (A.17) by the cell volume

$$\frac{d}{dt} \sum_{i \neq i_g} \overline{\rho_i} \alpha_i + \sum_{i \neq i_g} \frac{1}{\delta} \overline{\boldsymbol{u}_i \rho_i}^j f_i^j = 0 \,, \tag{A.18}$$

where α_i denotes the volume fraction of i in volume V_p, the index j marks the faces of the cell and f_i^j the surface fraction of the same constituent on the surface j bounding the volume. The quantity δ dividing the surface integrals represents the left over dimension of the cell volume. For example, the bulk zonal divergence of the mass flux becomes

$$\frac{1}{V_{pi}} \int_{S_{pi}} [u_i \rho_i(x^+) - u_i \rho_i(x^-)] dy dz = \frac{\overline{u_i \rho_i(x^+)} f_i^+ - \overline{u_i \rho_i(x^-)} f_i^-}{\delta_x} \,. \tag{A.19}$$

Clearly, to integrate ahead in time, exchanges between neighboring cells must be expressed in terms of known quantities, i.e., the volume averaged mean quantities. This is the parameterization problem of multiphase fluids expressed in the context of the mass equation and is representative of the artistry in multiphase modelling.

It is convenient at this point to compute also the budget V_p in of the mass of a single constituent. This reduces to the volume integration of a purely conservative quantity over a single index i. Further, the generalized flux of the mass consists only of an advective contribution and the fluids are immiscible. The result for a single constituent is

$$\frac{d}{dt} (\overline{\rho_i} \alpha_i) + \frac{1}{\delta} \sum_j \overline{\boldsymbol{u}_i \rho_i}^j f_i^j = 0 \,. \tag{A.20}$$

We now introduce a second simplification. We treat the mixture fluids as individually Boussinesq and collectively Boussinesq. The former constraint assumes

$$\frac{\delta \rho_{oil}}{\rho_{oil}} \ll 1; \quad \frac{\delta \rho_{water}}{\rho_{water}} \ll 1 \,, \tag{A.21}$$

both of which are familiar approximations. The 'collectively Boussinesq' assumption requires the stronger and less justifiable assertion that

$$\frac{\rho_{oil} - \rho_0}{\rho_0} \sim \frac{\rho_{water} - \rho_0}{\rho_0} \ll 1 \,. \tag{A.22}$$

The error introduced by the assumption inherent in (A.22) is about 10%. Although less justifiable than for single-phase water, 10% compares well

to the order of approximation in (A.16). If the above approximations are accepted, then the budget for mass of constituent i, where the index does not include gas, becomes

$$\frac{d}{dt}\alpha_i + \frac{1}{\delta}\sum_j \overline{\boldsymbol{u}_i}^j f_i^j = O\left(\frac{\rho_i - \rho_0}{\rho_0}\right) \ll 1\,, \tag{A.23}$$

while the total mass budget for the cell becomes

$$\frac{d}{dt}\sum_{i\neq i_g}\alpha_i + \frac{1}{\delta}\sum_{i\neq i_g,j}\overline{\boldsymbol{u}_i}^j f_i^j = O\left(\frac{\rho_i - \rho_0}{\rho_0}\right) \ll 1\,. \tag{A.24}$$

It will also be necessary for momentum reasons to monitor the mass of gas in a cell, the equation for which can be obtained by integration. The result is

$$\frac{d}{dt}(\overline{\rho_g}\alpha_g) + \frac{1}{\delta}\sum_j \overline{\boldsymbol{u}_g\rho_g}^j f_g^j = \frac{\partial}{\partial}M_g + \frac{1}{\delta}\sum_j \overline{\boldsymbol{u}_g\rho_g}^j f_g^j \tag{A.25}$$

where M_g mass per unit volume of gas. The gas density can be expected to vary given the strong pressure differences encountered during an ascent. Approximating the pressure by the static value of $p = \rho_0 gz$, the ideal gas law can be used to compute the gas density via

$$\frac{\rho_0\, gz}{RT} = \overline{\rho_g}\,. \tag{A.26}$$

Elaborations based on more accurate equations of state are also available. Computing M_g and dividing by ρ_g provides a prediction of α_g.

We now move to the momentum equations, the north-south one being

$$\frac{d}{dt}\sum_i \overline{(\rho_i v_i)}\alpha_i + f\sum_i \overline{(\rho_i u_i)}\alpha_i + \frac{1}{\delta}\sum_{i,j}\overline{(\rho_i \boldsymbol{u}_i v_i)}^j f_i^j + \frac{1}{\delta}\sum_{i,j}\overline{\mathbb{F}_i^{(y)}}^j f_i^j + \frac{\delta p}{\delta y} = 0 \tag{A.27}$$

The handling of the zonal momentum equation will mirror this, while the vertical momentum equation must be handled separately, as is typical for the Boussinesq equations. We again neglect the gases due to their small mass, which amounts to restricting (A.27) to not include the gas indices. The term

$$\frac{1}{\delta}\sum_{i,j}\overline{\mathbb{F}_i^{(y)}}^j f_i^j \tag{A.28}$$

denotes the aggregate impact of viscous effects and reduces to only those contributions occurring on the cell interfaces. This results from the requirement that all internal viscous exchanges between the liquids conserve momentum and the approximation that gas momentum is negligible. The use of the extended Boussinesq approximation in (A.27) allows it to be written as

$$\frac{d}{dt}\sum_{i\neq i_g}\overline{v_i}\alpha_i + f\sum_{i\neq i_g}\overline{u_i}\alpha_i + \frac{1}{\delta}\sum_{i\neq i_g,j}\overline{\boldsymbol{u}_i v_i}^j f_i^j + \frac{1}{\delta}\sum_{i\neq i_g,j}\overline{\mathbb{F}_i^{(y)}}^j f_i^j = O\left(\frac{\rho_{oi} - \rho_0}{\rho_0}\right) \ll 1\,, \tag{A.29}$$

where the reference oil and water densities are denoted by ρ_{oi}. Assuming adequate data is available at one time level, the result of applying (A.29) is a prediction for the oil and water volume weighted velocity (hereafter the composite velocity) associated with a point at the center of the V_v volume.

We now consider the volume averaged vertical momentum equation. Singling out the buoyancy and pressure terms,

$$-\frac{\delta p}{\delta z} - \sum_i \overline{\rho_i} g\alpha_i\,. \tag{A.30}$$

the usual procedure of removing the static pressure contribution returns

$$-\frac{\delta \hat{p}}{\delta z} - \sum_i (\overline{\rho_i} - \rho_0) g\alpha_i\,, \tag{A.31}$$

where $\hat{p}$ is the modified pressure (we will drop the hat in the following).

Following normal Boussinesq procedure, the density variations for the oil and water will be retained when multiplied by gravity. Note however that the gas produces a potentially huge contribution to the buoyancy due to its large mass deficit. Thus, while we can safely neglect the contribution of gas to momentum in any direction and to the mass of a cell, it cannot be neglected with regards to buoyancy forcing. Dividing the vertical momentum equation by the reference density, and neglecting the mass of the gas, the vertical momentum equation becomes

$$\frac{d}{dt}\sum_{i\neq i_g}\overline{w_i}\alpha_i + \frac{1}{\delta}\sum_{i\neq i_g,j}\overline{\boldsymbol{u}_i w_i}^j f_i^j - \widetilde{f}\sum_{i\neq i_g}\overline{u_i}\alpha_i + \frac{1}{\delta}\sum_{i\neq i_g,j}\overline{\mathbb{F}_i^{(z)}}^j f_i^j - \sum_i \overline{b_i} = 0\,, \tag{A.32}$$

with

$$\overline{b_i} = -g\frac{\overline{\rho_i} - \rho_0}{\rho_0}\,. \tag{A.33}$$

To this point, the substantive assumptions we have made are the extended Boussinesq character of the flows and the neglect of gas in computing cell mass and cell momentum. We could push further with this set, but it is useful and relatively benign to introduce another restriction. The gas will be assumed to be dilute, i.e., $\alpha_g << 1$. Admittedly, the initial DwH gas volume fraction was not small, but our calculations show it disperses quickly. Realistic net void fluxes can still be included into the problem by spreading the bubble flux over a large area. The value of neglecting the gas void fraction is that it avoids having to consider compression. In the mass equation (A.23) since $\alpha_g \ll 1$ the first term is comparable to the error and can be

neglected

$$\alpha_{oil} + \alpha_{water} = 1 - O(\alpha_{gas}) \sim 1\,. \tag{A.34}$$

The composite mass thus behaves like that of an incompressible fluid

$$\frac{1}{\delta}\sum_{i\neq i_g,j} \overline{\boldsymbol{u}_i}^{\,j} f_i^j = 0\,. \tag{A.35}$$

Now we consider the question of how to advance the model one-time step. For numerical calculations, the normal C-grid structure for the model lattice, with mass points at the center of a cube between meridional velocity points to the north and south, zonal velocity points to the east and west and vertical velocity points above and below, works well. The mass points are also the locations of tracer and volume fraction data. The cells around the velocity points are similarly defined. This is useful as many ocean models adopt C grid structure.

We assume gas volume fraction and one of the oil/water volume fractions and the oil and water velocities are known at some time level. From these and using (A.34) we can construct the composite velocity field. Recalling (A.35), a diagnostic equation involving a discrete analog of the Laplacian of the pressure can be formed. With surface exchanges expressed in terms of volume averages, the equation is closed and pressure can be computed. The composite momentum equations can now be integrated in time. The tracer and volume fraction equations are integrated with the assumption of fixed slip velocities in the vertical although this is not necessary. This essentially completes the discrete equation set.

A1. Conversion to partial differential equations

The multiphase equations derived above are in a form that lends itself to numerical computation. Our fluid mechanical intuition is more deeply rooted in partial differential equations, i.e. in the continuum limit. We here perform the conversion to PDEs adopting along the way suitable parameterizations for the exchanges between cells. We associate the volume averaged velocity and net buoyancy with the notation

$$\boldsymbol{U} = \sum_{i\neq i_g} \boldsymbol{u}_i\alpha_i, \quad B = -g\sum_{i\neq i_g}\frac{\rho_i-\rho_0}{\rho_0}\alpha_i - g\alpha_g\,. \tag{A.36}$$

To write the momentum equations, we need to parameterize the advective and diffusive momentum exchanges at the cell interface. Perhaps the simplest advective parameterization is

$$\sum_{i\neq i_g,j} \overline{\boldsymbol{u}_i\boldsymbol{u}_i}^{\,j} f_i^j = \nabla\cdot(\boldsymbol{U}\boldsymbol{U}) \tag{A.37}$$

which is equivalent to approximating momentum flux at the interface by using averages of the composite velocities. Doing essentially the same for the diffusive transfers yields the mixture momentum equations

$$\boldsymbol{U}_t + \nabla\cdot\boldsymbol{U}\boldsymbol{U} + \boldsymbol{f}\times\boldsymbol{U} = -\nabla p + B\boldsymbol{k} + \nabla\cdot D_U\cdot\nabla\boldsymbol{U}\,, \tag{A.38}$$

where D_U is a tensor controlling the amplitude of the diffusive fluxes. It is then consistent to write (A.35) as

$$\nabla\cdot\boldsymbol{U} = 0\,. \tag{A.39}$$

The tracer equations become

$$T_t + \nabla\cdot\boldsymbol{U}T = \nabla\cdot D_t\cdot\nabla T\,. \tag{A.40}$$

The distinctions between these equations and regular Navier–Stokes arises in the volume fraction equations, which are

$$\alpha_{it} + \nabla\cdot((\boldsymbol{U} + w_i\boldsymbol{k})\alpha_i) = \nabla\cdot D_\alpha\cdot\nabla\alpha_i\,, \tag{A.41}$$

$$\frac{\partial}{\partial t}M_g + \nabla\cdot((\boldsymbol{U} + w_g\boldsymbol{k})M_g) = \nabla\cdot D_\alpha\cdot\nabla M_g\,, \tag{A.42}$$

with the additional constraint

$$\sum_{i\neq i_g}\alpha_i = 1 \tag{A.43}$$

M_g is the mass distribution of the gas, given by $M_g = \overline{\rho_g}\alpha_g$ with gas density set nominally by the ideal gas law (A.26). The flux tensors for material X, D_X, must be parameterized in terms of the modelled variables and chemical/biological effects can appear on the right hand sides of the volume fraction equations.

References

Asaeda, T., Imberger, J., 1993. Structure of bubble plumes in linearly stratified environments. J. Fluid Mech. 35–57.

Batchelor, G., 1954. Heat convection and buoyant effects in fluids. Q. J. R. Meteorolog. Soc. 339–358.

Camilli, R., Iorio, D.D., Bowena, A., Reddy, C., Techet, A., Yoergera, D., Whitcomb, L., Seewald, J., Sylvac, S., Fenwick, J., 2012. Acoustic measurement of the Deepwater Horizon Macondo well flow rate. Proc. Natl. Acad. Sci. 20235–20239.

Camilli, R., Reddy, C., Yoerger, D., Van Mooy, B., Jakuba, M., Kinsey, J., cIntyre, C., Sylva, S., Maloney, J., 2010. Tracking hydrocarbon plume transport and biodegration at Deepwater Horizon. Science 330, 201–204.

Craske, J., van Reeuwijk, M., 2016. Generalised unsteady plume theory. J. Fluid Mech. 792, 1013–1052.

D'Asaro, E., Walker, S., Baker, E., 1994. Structure of two hydrothermal megaplumes. J. Geophys. Res. 99, 20361–20373.

Deremble, B., 2016. Convective plumes in rotating systems. J. Fluid Mech. 799, 27–55.

Deville, M.O., Fischer, P.F., Mund, E.H., 2002. High-Order Methods for Incompressible Fluid Flow. Cambridge University Press.

Fabregat, A., Dewar, W.K., Oezgoekmen, T.M., Poje, A.C., Wienders, N., 2015. Numerical simulations of turbulent thermal, bubble and hybrid plumes. Ocean Modell. 90, 16–28. http://dx.doi.org/10.1016/j.ocemod.2015.03.007.

Fabregat, A., Poje, A., Özgökmen, T., Dewar, W., 2016. Effects of rotation on turbulent buoyant plumes in stratified environments. J. Geophys. Res. http://dx.doi.org/10.1002/2016JC011737.

Fabregat, A., Poje, A.C., Özgökmen, T.M., Dewar, W.K., 2016. Dynamics of turbulent plumes with hybrid buoyancy sources in thermally stratified environments. Phys. Fluids. http://dx.doi.org/10.1063/1.4963313. *in press*

Fabregat, A., Poje, A.C., Özgökmen, T.M., Dewar, W.K., 2016. Effects of rotation on

turbulent buoyant plumes in stratified environments. J. Geophys. Res. http://dx.doi.org/10.1002/2016JC011737.
Fischer, P., Lottes, J., Kerkemeier, S., 2008a. Nek5000 web page. http://nek5000.mcs.anl.gov.
Fischer, P. F., Lottes, J. W., Kerkemeier, S. G., 2008b. Nek5000 web page. http://nek5000.mcs.anl.gov.
Fischer, P.F., Mullen, J.S., 2001. Filter-based stabilization of spectral element methods. Comptes rendus de lAcade mie des sciences Paris - Série I - Analyse numérique 332, 265–270.
Graham, B., Keilly, W., Beinecke, F., Boeach, D., Garcia, T., Marray, C., Ulme, F., 2011. Deep Water, The Gulf Oil Disaster and The Future of Offshore Drilling. Technical Report. US Government Printing Office.
Helfrich, K., Battisti, T., 1991. Experiments on baroclinic vortex shedding from hydrothermal plumes. J. Geophys. Res. 96, 12511–12518.
Hunt, G., Kaye, N., 2001. Virtual origin correction for lazy turbulent plumes. J. Fluid Mech. 435, 377–396.
Hunt, G., Kaye, N., 2005. Lazy plumes. J. Fluid Mech. 533, 329–338.
Johansen, O., 2000. DeepBlow - a Lagrangian plume model for deepwater blowouts. Spill Sci. Technol. Bull. 103–111.
Joyce, T., Stalcup, M., 1985. Wintertime convection in a Gulf Stream warm core ring. J. Phys. Oceanogr. 1032–1042.
Karamanos, G.-S., Karniadakis, G.E., 2000. A spectral vanishing viscosity method for large-eddy simulations. J. Comput. Phys. 163 (1), 22–50.
Koal, K., Stiller, J., Blackburn, H., 2012. Adapting the spectral vanishing viscosity method for large-eddy simulations in cylindrical configurations. J. Comput. Phys. 231 (8), 3389–3405.
Lehr, W., Bristol, S., Possolo, A., 2010. Oil Budget Calculator, Deepwater Horizon. Technical Report. The Federal Interagency Solutions Group.
Lemckert, C., Imberger, J., 1993. Energetic bubble plumes in arbitrary stratification. J. Hydraul. Eng. 119–125.
List, E., Imberger, J., 1973. Turbulent entrainment in buoyant jets and plumes. J. Hydraul. Div. (ASCE) 1461–1474.
Lubchenco, J., McNutt, M., Dreyfus, G., Murawski, S., Kennedy, D., Anastas, P., Chu, S., Hunter, T., 2012. Science in support of the Deepwater Horizon response. Proc. Natl. Acad. Sci. 20212–20221.
McDougall, T., 1978. Bubble plumes in stratified environments. J. Fluid Mech. 655–672.
McNutt, M., Chu, S., Lubchenco, J., Hunter, T., Dreyfus, G., Murawski, S., Kennedy, D., 2012. Applications of science and engineering to quantify and control the Deepwater Horizon oil spill. Proc. Natl. Acad. Sci. 20222–20228.
Morton, B., 1957. Buoyant plumes in a moist atmosphere. J. Fluid Mech. 127–144.
Morton, B., Taylor, G., Turner, J., 1956. Turbulent gravitational convection from maintained and instantaneous sources. Proc. R. Soc. London, Ser. A 24, 1–23.
Özgökmen, T.M., Iliescu, T., Fischer, P.F., 2009. Large eddy simulation of stratified mixing in a three-dimensional lock-exchange system. Ocean Modell. 26 (34), 134–155.
Özgökmen, T.M., Iliescu, T., Fischer, P.F., 2009. Reynolds number dependence of mixing in a lock-exchange system from direct numerical and large eddy simulations. Ocean Modell. 30 (23), 190–206.
Plume Modeling Team, 2010. Deepwater Horizon release estimate of rate by PIV. http://www.doi.gov/deepwaterhorizon/, Report to the Flow Rate Technical Group
Reddy, C., Arey, J., Seewald, J., Sylva, S., Lemkau, K., Nelson, R., Carmichael, C., McIntyre, C., Fenwick, J., Ventrua, G., Mooy, B.V., Camilli, R., 2012. Composition and fate of gas and oil released to the water column during the Deepwater Horizon oil spill. Proc. Natl. Acad. Sci. 20229–20234.
Rotunno, R., Emanuel, K., 1987. An air-sea interaction theory for tropical cyclones. J. Atmos. Sci. 44, 542–561.
Scase, M., Hewitt, R., 2012. Unsteady turbulent plume models. J. Fluid Mech. 697, 455–480.
Schmidt, W., 1941. Turbulent propagation of a stream of heated air. Z. Angew. Math. Mech. 265–351.
Sheremet, V., 2004. Laboratory experiments with tilted convective plumes on a centrifuge: a finite angle between the buoyancy force and the axis of rotation. J. Fluid Mech. 217–244.
Simiano, M., 2005. Experimental Investigation of Large-Scale Three Dimensional Bubble Plume Dynamics. Swiss Federal Institute of Technology, Zurich Ph.D. thesis.
Smagorinsky, J., 1963. General circulation experiments with the primitive equations. Mon. Weather Rev. 99–164.
Socolofsky, S., Adams, E., 2002. Multi-phase plumes in uniform and stratified crossflow. J. Hydraul. Res. 661–672.
Socolofsky, S., Adams, E., 2005. Role of slip velocity in the behavior of stratified multiphase plumes. J. Hydraul. Eng. 283–282
Socolofsky, S., Adams, E., Sherwood, C., 2011. Formation dynamics of subsurface hydrocarbon intrusions following the Deepwater Horizon blowout. Geophys. Res. Lett. 38. http://dx.doi.org/10.1029/2011GL047174.
Socolofsky, S., T. Bhaumik, T., Seol, D.-G., 2008. Double-plume integral models for near-field mixing in multiphase plumes. J. Hydraul. Eng. 772–783.
Socolofsky, S.A., Adams, E.E., Boufadel, M.C., Aman, Z.M., Johansen, O., Konkel, W.J., Lindo, D., Madsen, M.N., North, E.W., Paris, C.B., Rasmussen, D., Reed, M., Ronningen, P., Sim, L.H., Uhrenholdt, T., Anderson, K.G., Cooper, C., Nedwed, T.J., 2015. Intercomparison of oil spill prediction models for accidental blowout scenarios with and without subsea chemical dispersant injection. Mar. Pollut. Bull. 96 (1–2), 110–126. http://dx.doi.org/10.1016/j.marpolbul.2015.05.039.
Speer, K., Marshall, J., 1995. The growth of convective plumes at sea-floor hot-springs. J. Mar. Res. 1025–1057.
Spier, C., Stringfellow, W., Hazen, T., Conrad, M., 2013. Distribution of hydrocarbons released during the 2010 MC252 oil spill in deep offshore waters. Environ. Pollut. 173, 224–230.
Turner, J., 1973. Buoyancy Effects in Fluids. Cambridge University Press.
Woods, A., Bush, J., 1999. Dimensions and dynamics of megaplumes. J. Geophys. Res. 104, 20495–20507.
Zaker, N., Imberger, J., Pattiaratchi, C., 2001. Dispersion of an effluent plume in a shallow coastal area. J. Mar. Environ. Eng. 83–108.
Zeldovich, Y., 1937. The asymptotic laws of freely-ascending convective flows. J. Exp. Theor. Phys. (in Russian: English Translation 1992) 7, 1463–1465.
Zheng, L., Yapa, P., Chen, F., 2003. A model for simulating deepwater oil and gas blowouts - part I. Theory and model formulation. J. Hydraul. Res. 339–351.